

# Seismic anisotropy along the Haida Gwaii margin from receiver function analysis

Taylor A Tracey Kyryliuk<sup>1</sup>, Pascal Audet<sup>1</sup>, Jeremy M Gosselin<sup>1</sup>, and Andrew John Schaeffer<sup>2</sup>

<sup>1</sup>University of Ottawa

<sup>2</sup>Natural Resources Canada

November 24, 2022

## Abstract

Coastal British Columbia, Canada, has the highest seismic hazard in the country due to convergent and transpressive deformation at offshore plate boundaries between the Pacific, Juan de Fuca and North American plates. Further landward, the crust of the North American plate is made up of several geologically unique terranes and is unusually thin. Investigating the geophysical features in this area can help us better constrain its tectonic history and the geophysical processes that are currently underway. Here, we conduct an analysis of teleseismic body-wave scattering data (i.e. receiver functions) recorded at stations across western coastal British Columbia including northern Vancouver Island and southeastern Alaska. Using these receiver functions, we perform a harmonic decomposition with respect to earthquake back-azimuths to determine the orientation of seismic anisotropy over a series of depth ranges, attributable to either mineral alignment or dipping structures. We find a coherent pattern of margin-parallel orientations at upper crustal depths that persist onto the mainland at distances  $\sim 420$  km from the margin. Furthermore, dominant receiver function orientations at depth are attributed to dipping faults and interfaces, and fabrics due to lower crustal shearing or inherited from tectonic assembly along the margin. This work provides insight into the evolution of the margin and surrounding region, as well as the tectonic processes currently taking place. Identification of the dipping interfaces associated with the subducting Pacific and Juan de Fuca plates is important for assessment of earthquake and tsunami hazards.

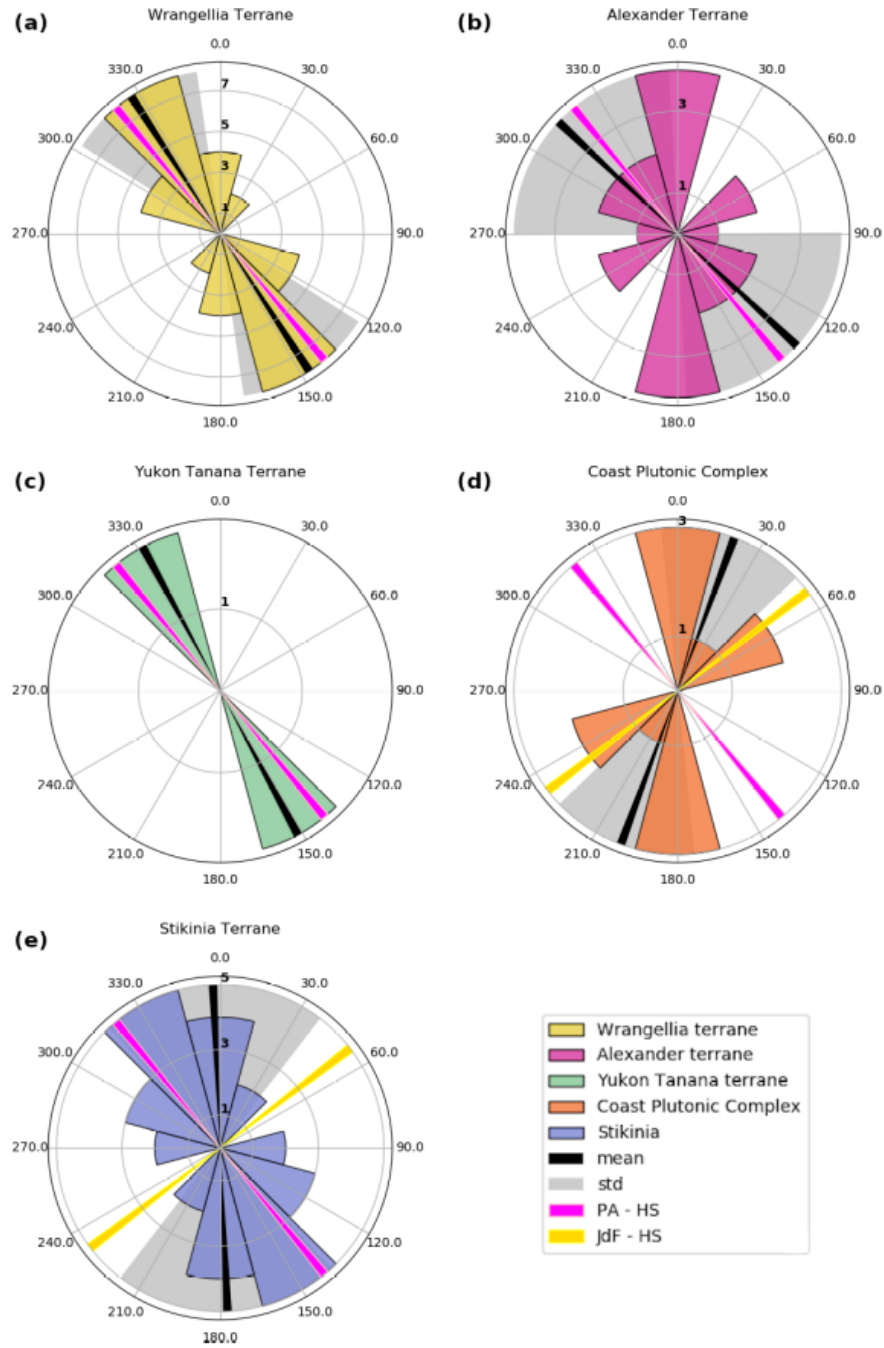


**Figure S1.** Rose diagrams showing the dominant orientations of the receiver functions for the 5 - 15 km depth range grouped by terrane. Plot (a) shows the Wrangellia terrane, (b) Alexander terrane, (c) Yukon Tanana terrane, (d) Coast Plutonic Complex, (e) Stikinia terrane. The circular mean azimuths are plotted as a thick black line with the standard deviation on that value shown in light gray on each subplot. The directions of the PA and JdF relative to the global hotspot are plotted in pink and yellow respectively.

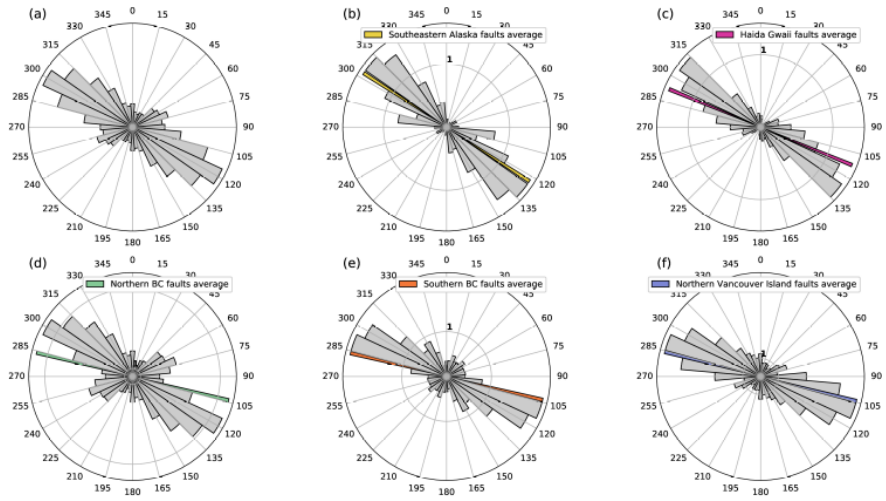


**Figure S2.** Rose diagrams of regional fault orientations. (a) shows all faults within the study area, (b) shows southeastern Alaska, (c) shows Haida Gwaii, (d) shows northern BC, (e) shows southern BC and (f) shows northern Vancouver Island. Coloured bars represent the circular mean of the faults weighted by their lengths.

1 **Crustal seismic anisotropy along the continental margin**  
2 **in western Canada from receiver function analysis**

3 **T. Tracey Kyryliuk<sup>1</sup>, P. Audet<sup>1</sup>, J. M. Gosselin<sup>1,2</sup>, and A. J. Schaeffer<sup>3</sup>**

4 <sup>1</sup>Department of Earth and Environmental Science, University of Ottawa, Ottawa, ON, K1N 6N5

5 <sup>2</sup>Now at Department of Geoscience, University of Calgary, Calgary, AB, T2N 1N4

6 <sup>3</sup>Geological Survey of Canada, Natural Resources Canada, Sidney, BC, V8L 4B2

7 **Key Points:**

- 8 • Receiver functions are calculated for 74 broadband 3-component seismic stations  
9 across coastal British Columbia.
- 10 • We detect signs of seismic anisotropy beneath all stations in our study.
- 11 • Seismic anisotropy is attributed to changes in Moho depth, faults, and pervasive  
12 deformation-related fabrics.

---

Corresponding author: T. Tracey Kyryliuk, [ttrac015@uottawa.ca](mailto:ttrac015@uottawa.ca)

**Abstract**

Coastal British Columbia, Canada, has the highest seismic hazard in the country due to convergent and transpressive deformation at offshore plate boundaries between the Pacific, Juan de Fuca and North American plates. Further landward, the crust of the North American plate is made up of several geologically unique terranes and is unusually thin. Investigating the geophysical features in this area can help us better constrain its tectonic history and the geophysical processes that are currently underway. Here, we conduct an analysis of teleseismic body-wave scattering data (i.e, receiver functions) recorded at stations across western coastal British Columbia including northern Vancouver Island and southeastern Alaska. Using these receiver functions, we perform a harmonic decomposition with respect to earthquake back-azimuths to determine the orientation of seismic anisotropy over a series of depth ranges, attributable to either mineral alignment or dipping structures. We find a coherent pattern of margin-parallel orientations at upper crustal depths that persist onto the mainland at distances 420 km from the margin. Furthermore, dominant receiver function orientations at depth are attributed to dipping faults and interfaces, and fabrics due to lower crustal shearing or inherited from tectonic assembly along the margin. This work provides insight into the evolution of the margin and surrounding region, as well as the tectonic processes currently taking place. Identification of the dipping interfaces associated with the subducting Pacific and Juan de Fuca plates is important for assessment of earthquake and tsunami hazards.

**Plain Language Summary**

Coastal British Columbia is a geologically complex region, but could it also be the epicenter of large tsunami causing earthquakes that put the lives of residents all around the Pacific at risk? Better understanding how this region formed and the current geometry of the tectonic plates can help us address this question. We study seismic waves from distant earthquakes recorded at over 60 seismometers distributed across western British Columbia to see if wave speeds depend on the direction from which the earthquake approaches. This directional dependence could be caused by a dipping boundary between two different media in the Earth's crust/mantle or by a directional dependence in properties of the material the wave travels through. We detect directional dependency in seismic wave speeds beneath all seismometers in our study at multiple depths in the Earth's crust/uppermost mantle. From this data set we determine the strike of dipping bound-

aries and/or the trend of material properties, coming from various sources such as changes in the thickness of the crust, faults, and material fabrics caused by deformation. Results of this study add to the body of knowledge of the formation history of western British Columbia and the assessment of earthquake and tsunami hazards.

## 1 Introduction

The continental margin of British Columbia (BC), in western Canada, is a geologically complex region due to its tectonic history and modern tectonic regime. This region is currently characterized by a plate boundary system that transitions from subduction in the south to transform motion in the north. On Vancouver Island, the Cascadia subduction zone defines underthrusting of the the Juan de Fuca (JdF) plate beneath the North American (NA) plate. North of the Cascadia subduction zone, the region is comprised of a poorly defined and evolving triple junction between NA, the Pacific (PA) plate and the Explorer (Ex) microplate. Further north, the plate boundary between PA and NA evolves into the dextral transform Queen Charlotte Fault (QCF). The Haida Gwaii archipelago marks the transition between the triple junction and the transform system, although the exact nature of the boundary between the PA and NA plates in this region remains ambiguous (Hyndman & Ellis, 1981; Rohr et al., 2000; Smith et al., 2003; ten Brink et al., 2018). Currently, there is non-zero convergence of  $\sim 15$  mm/year between the two plates due to the transpressive nature of the margin along the restraining southern part of the QCF (DeMets & Dixon, 1999; DeMets et al., 2010; Schoettle-Greene et al., 2020). Seismic, thermal and other geophysical evidence suggest that the convergence is accommodated by oblique underthrusting of the PA plate beneath Haida Gwaii (Smith et al., 2003; Bustin et al., 2007; Lay et al., 2013; Gosselin et al., 2015; Hyndman, 2015; ten Brink et al., 2018). The landward extent of underthrusting of the PA plate beneath NA is currently unknown (Smith et al., 2003; ten Brink et al., 2018); resolving this question is important for seismic hazard and tectonic reconstruction models.

Further landward, the geology changes relatively little along the strike of the margin (Monger, 1993) but from west to east, the mainland is characterized by a collage of accreted and deformed exotic terranes. These terranes are grouped into two superterranes defined by two accretionary episodes and are separated by the margin-parallel crustal scale Coast Shear Zone (CSZ). The Coast Plutonic Complex (CPC) was intruded into

77 this shear zone during long-lived subduction-related arc magmatism and exhumation along  
78 the margin (Hollister & Andronicos, 2006). The surficial geology of this region is rela-  
79 tively well studied (Nelson et al., 2007, 2013) and efforts have been made to constrain  
80 its crustal structure and fabrics by means of geophysical data (Hammer et al., 2000; Mo-  
81 rozov et al., 2001; Hollister & Andronicos, 2006; Calkins et al., 2010). Results of these  
82 studies show that the Moho dips from west to east to a depth of up to 37 km beneath  
83 the easternmost terrane (inland) and the mantle-lithosphere boundary is between 60-  
84 70 km depth (Hollister & Andronicos, 2006; Calkins et al., 2010).

85 Seismic anisotropy is the directional dependence of seismic wave propagation, and  
86 is one of the best tools to study the structure and fabrics of the crust (Babuska & Cara,  
87 1991). In particular, anisotropy characterized using teleseismic receiver functions (RFs)  
88 can be used to constrain the geometry and seismic velocities across dipping interfaces,  
89 and/or rock fabrics from large-scale mineral alignment in the crust (e.g., Levin & Park,  
90 1997; Savage, 1998a). The goal of this paper is to use RFs to investigate variations in  
91 seismic anisotropy along the continental margin of BC. In particular, we use RFs to search  
92 for evidence of dipping structures or material anisotropy at a range of crustal depths,  
93 and interpret these observations in relation to modern and past geodynamic environments.

94 A handful of studies have previously examined crustal structure using RFs in west-  
95 ern Canada, although none of them considered the broader context of the entire conti-  
96 nental margin. Notably, RFs were used to study the extent of subduction beneath north-  
97 ern Cascadia (Audet et al., 2008), underthrusting beneath Haida Gwaii (Smith et al.,  
98 2003; Bustin et al., 2007; Gosselin et al., 2015), and the architecture of the crust across  
99 the CPC (Calkins et al., 2010). However, these studies did not examine back-azimuth  
100 (BAZ) variations in RF signals and therefore could not resolve seismic anisotropy. Lastly,  
101 significant expansion of regional seismic networks in this area occurred following the moment-  
102 magnitude 7.8 thrust earthquake and associated tsunami off the west coast of Haida Gwaii  
103 in 2012 (Cassidy et al., 2014; Leonard & Bednarski, 2014), further motivating additional  
104 RF studies in the region.

105 Other previous seismic studies of crustal structure and fabrics include local shear-  
106 wave splitting on Haida Gwaii (Cao et al., 2017) and southern Vancouver Island and sur-  
107 rounding area (Balfour et al., 2012), surface wave tomography (Gosselin et al., 2020),  
108 and seismic reflection along the Portland Canal in BC (Morozov et al., 1998). We use

109 observations and conclusions from these past studies to interpret our own results in light  
110 of the dominant orientations of previously recognized geological and geophysical features.  
111 We also consider how these features evolve landward from the Haida Gwaii margin and  
112 as a function as depth. These results give further insight into the past and present tec-  
113 tonic regime of the Haida Gwaii margin and surrounding geological units.

## 114 **2 Tectonic Setting and History**

115 The tectonics of the Cordillera in western Canada throughout the Mesozoic are dom-  
116 inated by the interactions between the now defunct Kula and Farallon plates with the  
117 PA and NA plates (Engebretson et al., 1984; ten Brink et al., 2018). The continent-ocean  
118 boundary is considered to have initiated in the late Proterozoic and continued to evolve  
119 throughout the Phanerozoic (Monger, 1993). Our particular study area is comprised of  
120 five geomorphologically distinct regions from west to east: the Wrangellia terrane, the  
121 Alexander terrane, the Yukon-Tanana terrane (YTT) (also sometimes referred to as Taku),  
122 the CPC and the Stikinia terrane. Continental growth by accretion of the terranes likely  
123 occurred in two episodes (Gabrielse et al., 1991). First, the Intermontane superterrane,  
124 which includes Stikinia and YTT, is believed to have thrust eastward onto the NA plate  
125 during dextral transpression some time during the Jurassic (Hammer et al., 2000). Next,  
126 the Insular superterrane, containing the Wrangellia and Alexander terranes, is believed  
127 to have been thrust onto the NA plate during sinistral transpression in the mid-Cretaceous  
128 (Chardon et al., 1999; Hammer et al., 2000). This second accretionary episode is also  
129 considered a contributor to deformation of the Intermontane superterrane (Hammer et  
130 al., 2000).

131 The result of the proposed history of large-scale transpression along western NA  
132 is a juxtaposition of distinct crustal materials separated by shear zones and northwest  
133 striking crustal scale fault systems (Chardon et al., 1999; ten Brink et al., 2018). A mid-  
134 Cretaceous thrust belt west of the CPC extends from the surface down to the mantle  
135 (Hollister & Andronicos, 2006). This feature is expressed as an offset in Moho depth (Hollister  
136 & Andronicos, 2006; Calkins et al., 2010).

137 Concurrent with the transpressive motion, prolonged subduction of the Kula-Farallon  
138 plate system under NA would have generated a continental magmatic arc in the shear  
139 zone between the two superterranes, possibly in two episodes (Engebretson et al., 1984;

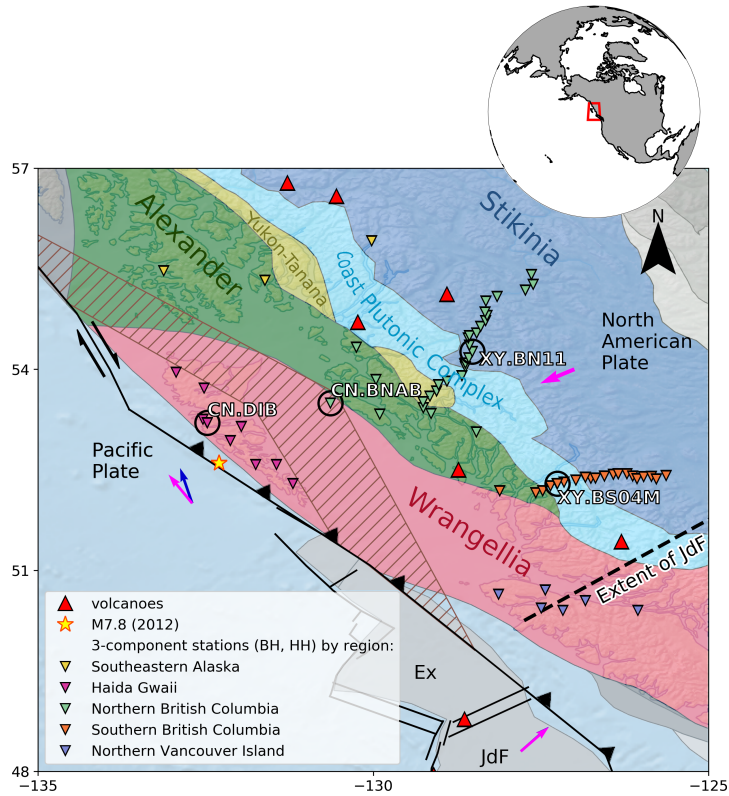


**Figure 1.** Map of the study area. The estimated absolute and relative motions of the plates are shown as colored vectors, based on the Hotspot reference frame (magenta) and relative to NA (blue) (Gripp & Gordon, 2002). The brown hatched polygon outlines the possible landward extent of the subducted PA slab (Smith et al., 2003). Dashed line shows the approximate northern terminus of JdF plate subduction (Savard et al., 2020). Stations are colour-coded by regional sets. Stations with RF analysis shown in subsequent figures are circled and labeled. The epicentre of the 2012 earthquake is marked with a star. Terranes relevant to this study are highlighted and labelled by colour.

140 Calkins et al., 2010; ten Brink et al., 2018). During the first episode, subduction related  
 141 partial melting and mixing would have resulted in the emplacement of plutons within  
 142 the shear zone (Hollister & Andronicos, 2006). The relative change in plate motions in  
 143 the early Eocene would then have caused a period of crustal extension, moving the up-  
 144 per crust of the shear zone onto Stikinia and exhuming the plutons, creating the CPC  
 145 (Hollister & Andronicos, 2006) and forming a northeast foliated, northeast dipping, duc-  
 146 tile shear zone on the eastern boundary between the CPC and Stikinia (Andronicos et

147 al., 2003). Several of these felsic plutons within the CPC appear to be sill-like or domed  
148 in shape (Hollister & Andronicos, 2006).

149       Eventual subduction of the spreading ridge between the Kula and Farallon plates  
150 would have then led to the development of a slab window, well established by the early  
151 Miocene and believed to currently encompass southeastern Alaska to southwest BC (Thorkelson  
152 & Taylor, 1989). This slab window is linked with the generated intraplate volcanism within  
153 a hot and thin lithosphere (Thorkelson et al., 2011). It is suggested that the Kula plate  
154 was captured by the PA early-mid Eocene and began the predominantly right-lateral mo-  
155 tion seen today along the QCF (ten Brink et al., 2018). Upon complete subduction of  
156 the ridge, the triple junction between the PA, NA plates and JdF plate (the remnant of  
157 the Farallon plate) would have moved south to its current location (Thorkelson & Tay-  
158 lor, 1989).

159       The modern configuration of tectonic plates is shown in Figure 1. The continen-  
160 tal margin of NA extends to the western coast of Haida Gwaii, where it meets the PA  
161 near the dextral transform QCF, which is among Canada’s most seismically active re-  
162 gions (Hyndman & Ellis, 1981; Bird, 1999). To the north, the QCF transitions into the  
163 Fairweather Fault in southeastern Alaska. The NA-PA-Ex triple junction is poorly de-  
164 fined and is situated somewhere between the northern end of Vancouver Island and south-  
165 ern Haida Gwaii (Savard et al., 2020). The Ex plate accommodates the relative motions  
166 of the NA, PA and JdF plates and its separation from the JdF plate is attributed to ther-  
167 momechanical erosion of the slab edge and thinning of the slab (Audet et al., 2008). To  
168 the south of the triple junction, subduction of the JdF plate beneath NA defines the Cas-  
169 cadia subduction zone. Above this portion of the subduction zone, clockwise rotation  
170 of the Oregon block drives the west coast of the United States northward (McCaffrey  
171 et al., 2000; Balfour et al., 2012).

172       Along Haida Gwaii, the motion of the PA plate relative to NA is 338° clockwise  
173 from north. The direction of plate motion with respect to the orientation of the mar-  
174 gin (Fig. 1) results in convergence of  $\sim 15 \text{ mm yr}^{-1}$  (Gripp & Gordon, 2002), which is  
175 accommodated by either crustal thickening or oblique subduction of the PA slab beneath  
176 NA (Smith et al., 2003). In 2012, a  $M_W=7.8$  earthquake with a dominant thrust com-  
177 ponent occurred at the Haida Gwaii margin (Cassidy et al., 2014), confirming that the  
178 plate boundary fault dips beneath Haida Gwaii. Plate kinematics place the landward

179 extent of potential underthrusting of the PA plate beneath Hecate Strait (east of Haida  
180 Gwaii; Figure 1). However, the exact limit depends on the time of subduction initiation  
181 as well as the location of the triple junction at that time (Smith et al., 2003), both of  
182 which are uncertain. Seismic evidence of the downward extent of the PA slab is limited  
183 (Bustin et al., 2007; Gosselin et al., 2015, 2020), and the extent of possible subduction  
184 is currently unresolved.

### 185 **3 Methodology**

#### 186 **3.1 Receiver functions**

187 At teleseismic distances, direct P-waves from moderate (magnitude  $M > 5.5$ ) earth-  
188 quakes arrive before any other body-wave phase, and can be approximated as a nearly  
189 vertically propagating plane wave incident beneath a recording station. The incoming  
190 P wave interacts with subsurface seismic velocity discontinuities and produces P-to-S con-  
191 verted phases that are projected onto the horizontal components of motion. By approx-  
192 imating the vertical-component P-wave seismogram as a source wavelet incident on the  
193 receiver-side structure, we can deconvolve it from the horizontal components and pro-  
194 duce a so-called RF that isolates the P-to-S conversions. Consequently, RFs are approx-  
195 imations to the Earth’s impulse response, and provide a valuable constraint on one-dimensional  
196 seismic velocity structure beneath a seismic station (Langston, 1977, 1979; Cassidy, 1992;  
197 Savage, 1998b). The timing of the phases in the RF can be used to infer the depth of  
198 the seismic velocity discontinuities that produced them, and the amplitudes of the phases  
199 can be used to infer the magnitude of the contrast in seismic velocities across the dis-  
200 continuities.

201 For a horizontally layered isotropic medium, P-to-S converted energy is constrained  
202 to the radial plane (i.e., in line with the distant earthquake). However, in the presence  
203 of dipping layers and/or material anisotropy, P-to-S converted energy can be projected  
204 out of the radial plane and onto the transverse component of motion. Consequently, the  
205 presence of coherent arrivals on transverse-component RFs is indicative of dipping struc-  
206 ture and/or material anisotropy beneath a seismic station (Cassidy, 1992; Savage, 1998b).  
207 The amplitude, polarity and timing of RF phases vary smoothly with respect to the BAZ  
208 of the event used to produce the RF (Porter et al., 2011). This directional dependence  
209 can be used to infer the geometry and orientation of complex subsurface structure by

210 modelling sinusoidal variations in RF phases (e.g., Bianchi et al., 2010; Porter et al., 2011;  
 211 Schulte-Pelkum & Mahan, 2014; Audet, 2015).

### 212 3.2 Harmonic decomposition

213 In this work, we decompose the RF data at each station into low-order periodic func-  
 214 tions (i.e., harmonics). Specifically, a set of  $N$  radial  $R_V$  and transverse  $R_T$  RFs at a  
 215 given station can be decomposed into five harmonic components according to:

$$\begin{pmatrix} R_{V1}(z) \\ \vdots \\ R_{VN}(z) \\ R_{T1}(z) \\ \vdots \\ R_{TN}(z) \end{pmatrix} = \begin{pmatrix} 1 & \cos(\phi_1 - \alpha) & \sin(\phi_1 - \alpha) & \cos(2(\phi_1 - \alpha)) & \sin(2(\phi_1 - \alpha)) \\ \vdots & \vdots & \vdots & \vdots & \vdots \\ 1 & \cos(\phi_N - \alpha) & \sin(\phi_N - \alpha) & \cos(2(\phi_N - \alpha)) & \sin(2(\phi_N - \alpha)) \\ 0 & \cos(\phi_1 - \alpha + \frac{\pi}{2}) & \sin(\phi_1 - \alpha + \frac{\pi}{2}) & \cos(2(\phi_1 - \alpha) + \frac{\pi}{4}) & \sin(2(\phi_1 - \alpha) + \frac{\pi}{4}) \\ \vdots & \vdots & \vdots & \vdots & \vdots \\ 0 & \cos(\phi_N - \alpha + \frac{\pi}{2}) & \sin(\phi_N - \alpha + \frac{\pi}{2}) & \cos(2(\phi_N - \alpha) + \frac{\pi}{4}) & \sin(2(\phi_N - \alpha) + \frac{\pi}{4}) \end{pmatrix} \begin{pmatrix} A(z) \\ B_{\parallel}(z) \\ B_{\perp}(z) \\ C_{\parallel}(z) \\ C_{\perp}(z) \end{pmatrix}, \quad (1)$$

216 where  $\phi_i$  is the BAZ of the  $i$ -th event. The harmonic term  $A$  is the mean of the radial  
 217 component RFs, and represents the signal in the data due to isotropic structure.  $B_{\parallel}$  and  
 218  $B_{\perp}$  are the first harmonic terms, and describe signal in the RF dataset that varies with  
 219  $2\pi$  periodicity over BAZ, which has been shown to be attributed to dipping interfaces  
 220 and anisotropic materials with a plunging axis of hexagonal symmetry (e.g., Porter et  
 221 al., 2011; Schulte-Pelkum & Mahan, 2014). Similarly,  $C_{\parallel}$  and  $C_{\perp}$  correspond to signals  
 222 that arise from anisotropic materials with a horizontal axis of symmetry, which display  
 223 a  $\pi$  periodicity in RFs (Bianchi et al., 2010; Audet, 2015). Unfortunately, the ability to  
 224 accurately constrain these higher-order harmonic terms is typically limited by the az-  
 225 imuthal sampling of the RF dataset. However, we note in Equation 1 the predicted az-  
 226 imuthal shift for the transverse component relative to the radial component, which has  
 227 the effect of improving the azimuthal coverage.

228 Note that  $R_V$  and  $R_T$  represent the time-to-depth converted radial and transverse  
 229 components, respectively. We discuss the depth conversion processing further below. Lastly,  
 230  $\alpha$  represents the rotation angle of the harmonic reference frame. In a geographic refer-  
 231 ence frame ( $\alpha = 0$ ), the coordinate system of the BAZ harmonics is aligned with the  
 232 north-south and east-west directions (Bianchi et al., 2010). Instead, an angle  $\alpha$  that max-  
 233 imizes signal variance on a specific harmonic component can be estimated in order to  
 234 infer the alignment of structural features beneath a seismic station (Audet, 2015). In this  
 235 work, we estimate  $\alpha$  by maximizing signal on the  $B_{\perp}$  component. Under this frame ro-

236 tation,  $\alpha$  represents the strike of a dipping layer or the trend of a dipping orientation in  
 237 anisotropic rocks (Audet, 2015).

### 238 **3.3 Data processing**

239 Our dataset comprises 74 broadband, 3-component seismograph stations distributed  
 240 over Haida Gwaii, southeastern Alaska, northern Vancouver Island, and coastal BC (up  
 241 to  $\sim 420$  km landward) (Fig. 1). We separate coastal BC into southern and northern por-  
 242 tions. These five regions are used to group RF results to describe regional structure.

243 We calculate RFs for all available data from earthquakes with moment magnitude  
 244 greater than 5.8 during operation time of the stations. We use the iasp91 velocity model  
 245 (Kennett & Engdahl, 1991) to download 120 second seismograms centered on the pre-  
 246 dicted P, or PP, arrival. We consider events over  $30 - 90^\circ$  and  $100 - 160^\circ$  degrees in epi-  
 247 central distance for P and PP arrivals, respectively. We calculate the signal-to-noise (SNR)  
 248 ratio relative to pre-arrival noise over the initial 30 s following the predicted arrival on  
 249 the vertical component, filtered over the frequency range 0.05 - 1.0 Hz. We only consider  
 250 data with SNR above 5.0 dB for further analysis. Next, we rotate the horizontal com-  
 251 ponents to radial and transverse orientations relative to event locations (i.e., BAZ). RFs  
 252 are then calculated using the multi-taper method in order to deconvolve the vertical com-  
 253 ponent from the horizontal components (Park & Levin, 2000). The resulting high-quality  
 254 RFs are then band-pass filtered between 0.05 and 0.8 Hz, binned by slowness and BAZ,  
 255 and then migrated to depth using a 1D seismic velocity model provided by the Geolog-  
 256 ical Survey of Canada (Canadian Hazards Information Service, 2021). This initial bin-  
 257 ning is performed in order to improve the computational efficiency of the depth migra-  
 258 tion. Subsequently, the depth-migrated RFs are binned into 72 BAZ bins. Lastly, we vi-  
 259 sually inspect the RF data at each station. Those that exhibit RF data with significant  
 260 and/or uncharacteristic noise, or contain significant azimuthal gaps in data coverage (less  
 261 than  $50^\circ$  of coverage), are not considered for further analysis.

262 For each station, we perform a harmonic decomposition in order to estimate the  
 263  $\alpha$  parameter (equation 1) that minimizes the variance on the  $B_{\parallel}$  harmonic component  
 264 (i.e., maximizes variance on  $B_{\perp}$ ) over a specific depth range for which we assume  $\alpha$  to  
 265 be constant. We perform this analysis for several overlapping depth ranges that are 10 km  
 266 thick, from 5 to 50 km with a 5 km overlap. Previous studies suggest shallow Moho depths

267 of  $\sim 32$  km over much of western BC (Cook et al., 2010; Tarayoun et al., 2017), and 18-  
 268 26 km beneath Haida Gwaii (Gosselin et al., 2015). Our analysis investigates structure  
 269 through the entire crust. However, minimizing the  $B_{\parallel}$  variance over 10 km-thick depth  
 270 windows reduces the vertical resolution of our results. Lastly, we perform bootstrap re-  
 271 sampling of the RF data at each station, and repeat the harmonic analysis for each boot-  
 272 strap sample, in order to estimate  $1-\sigma$  uncertainty on our estimated  $\alpha$  values. Results  
 273 with uncertainty greater than  $36^\circ$  are not considered in our interpretations.

## 274 4 Results

### 275 4.1 Examples at single stations

276 Figure 2 shows examples of RF processing and harmonic analysis for stations lo-  
 277 cated on Haida Gwaii (DIB), southern BC (BS04M), northern BC (BN11) and Hecate  
 278 Strait (BNAB) (Fig. 1). All stations display a gap in the RF coverage between  $180^\circ$  and  
 279  $220^\circ$  BAZ due to the paucity of global earthquakes at those BAZ. Stations DIB and BNAB  
 280 have accumulated several years of high-quality data and display excellent coverage in BAZ.  
 281 Stations BN11 and BS04M are part of a temporary network and display a sparser cov-  
 282 erage in BAZ with significant gaps between  $40^\circ$  and  $120^\circ$ , due to their limited deploy-  
 283 ment duration. At all stations, we find periodic variations in amplitude with BAZ in both  
 284 the radial and transverse components of RFs, which are indicative of seismic anisotropy  
 285 and/or dipping structure beneath these stations (e.g., Fig. 2).

286 Figure 3 shows the harmonic components for stations DIB (a) and BNAB (b). For  
 287 these examples, the angle  $\alpha$  (equation 1) and the resulting components are calculated  
 288 and shown for a selected depth range that encompasses the largest amplitude of the RF  
 289 signals. Note the minimization of signal variance on the  $B_{\parallel}$  components within the spe-  
 290 cific depth range, and the corresponding large signal variance on the  $B_{\perp}$  components.  
 291 Solving for  $\alpha$ , as well as the corresponding signal variance on the  $B_{\perp}$  component, over  
 292 various depth ranges allows us to infer changes in the alignment and relative signal strength  
 293 of dipping structure or anisotropy beneath a seismic station as a function of depth. The  
 294 magnitude of the variance on  $B_{\perp}$  represents the relative strength of anisotropic and/or  
 295 dipping structures over the specified depth range, for the estimated orientation (Audet,  
 296 2015). For station DIB (Fig. 3(a)), there is large variance on the  $B_{\parallel}$  component but off-  
 297 set in depth from  $B_{\perp}$  indicating the presence of multiple sources with different orienta-

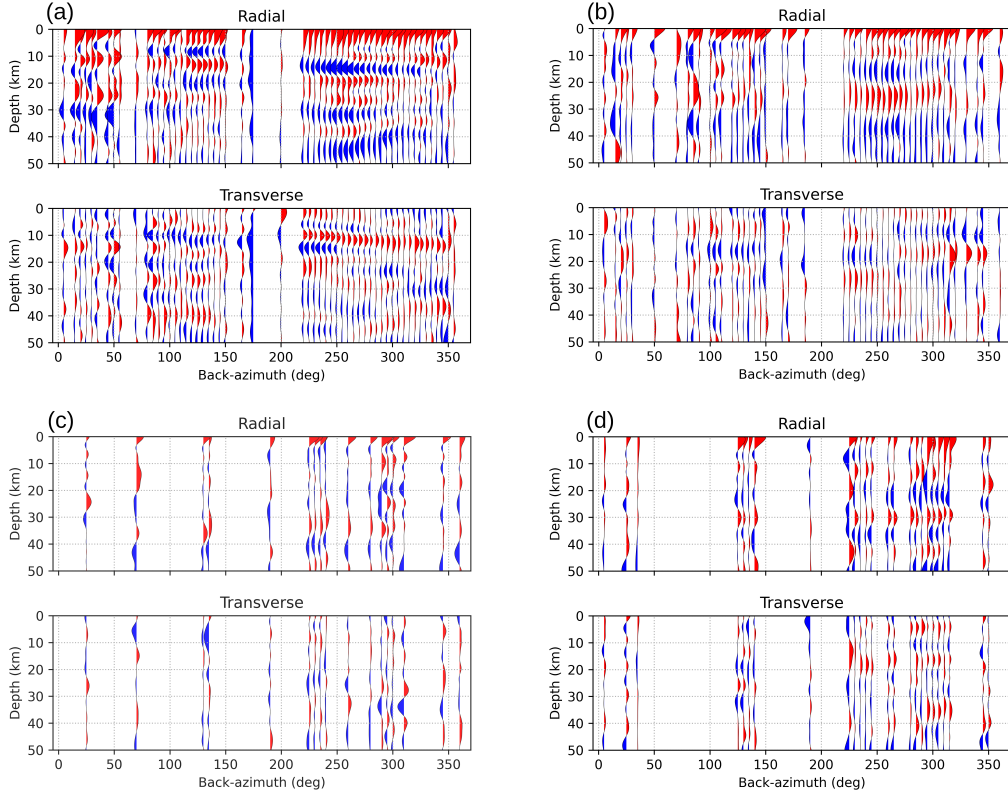


**Figure 2.** Examples of RF at stations DIB (a), BNAB (b), BN11 (c) and BS04M (d). These stations are circled and labelled in Figure 1. Radial (top panel) and transverse (bottom panel) RFs in each case are plotted from 0 to 50 km depth and sorted in BAZ bins.

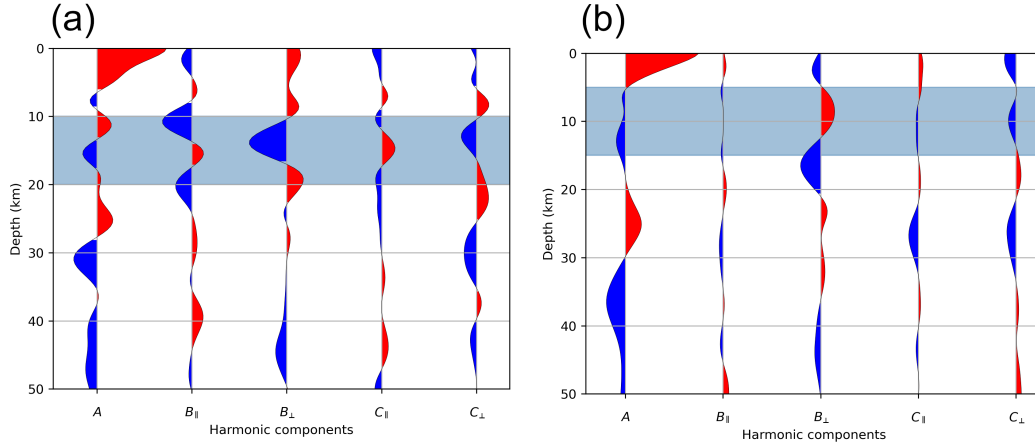


**Figure 3.** Examples of harmonic component analysis at corresponding stations DIB with  $\alpha = 2 \pm 5^\circ$  (a) and BNAB with  $\alpha = 332 \pm 4^\circ$  (b) in Figure 2. The decomposition is performed at the azimuth which minimizes the variance of the  $B_{\parallel}$  component within the depth range highlighted by the grey shading. The five components are plotted from 0 to 50 km depth. Note the greater signal variance on the  $B_{\perp}$  component within the shaded depth range.

298 tions contributing to this signal. Although the  $C$  components are also estimated and pro-  
 299 vide some constraint on azimuthal anisotropy, accurate estimation of these components  
 300 requires greater RF data coverage over event BAZ (as discussed previously). Since such  
 301 azimuthal coverage is highly variable between stations considered in this work due to dif-  
 302 ferences in geographic location and station deployment duration, we do not consider the  
 303  $C$  components further.

## 304 4.2 Spatial variations

305 We map the spatial distribution of  $\alpha$  for each 10 km depth range as oriented bars  
 306 scaled by the magnitude of the variance on the  $B_{\perp}$  component, and show the error in  
 307  $\alpha$  as shaded bow ties (Fig. 4). At this scale, we observe a general NW-SE alignment at  
 308 some depth ranges that follows the trend of terrane boundaries, but no obvious cluster-  
 309 ing of  $\alpha$  by terrane (Fig. S1). Instead of examining results for separate geological units,  
 310 we group results into the regional sets shown in Figure 1: southeastern Alaska, Haida  
 311 Gwaii, northern BC, southern BC and northern Vancouver Island. These results are dis-  
 312 played as density estimates for the magnitude, orientation (azimuth difference with the  
 313 PA plate motion) and standard deviation estimated for each depth range (Fig. 5).

314 Within the depth range of 5 - 15 km (Fig. 4(a)),  $\alpha$  estimates are consistently ori-  
 315 ented NW-SE over the entire region, with the overall magnitude of the signals being larger  
 316 and more narrowly distributed than any other depth range. This is in general agreement  
 317 with the strike of terrane boundaries and the directions of both the absolute and rela-  
 318 tive PA plate motion (Gripp & Gordon, 2002; Kreemer et al., 2014). Using rose diagrams,  
 319 we determine the dominant RF orientations at this depth range and show the mean and  
 320 standard deviation of  $\alpha$  for the entire dataset and for each sub-region (Fig. 6). Compar-  
 321 ing the sub-regions for this depth range from SE to NW (Fig. 4(a)), we observe a slight  
 322 rotation in the orientation from  $338^{\circ}$  beneath northern Vancouver Island and southern  
 323 BC to  $\sim 320^{\circ}$  beneath Haida Gwaii and northern BC, and then to  $353^{\circ}$  beneath south-  
 324 eastern Alaska.

325 Below the 5 - 15 km depth range,  $\alpha$  values on the mainland exhibit complex pat-  
 326 terns, with some locally coherent orientations. In southeastern Alaska,  $\alpha$  values are ro-  
 327 tated  $\sim 30^{\circ}$  clockwise from the PA plate motion within the 35 - 45 km depth range. Es-  
 328 timated  $\alpha$  values beneath Haida Gwaii switch orientations between different depth ranges.

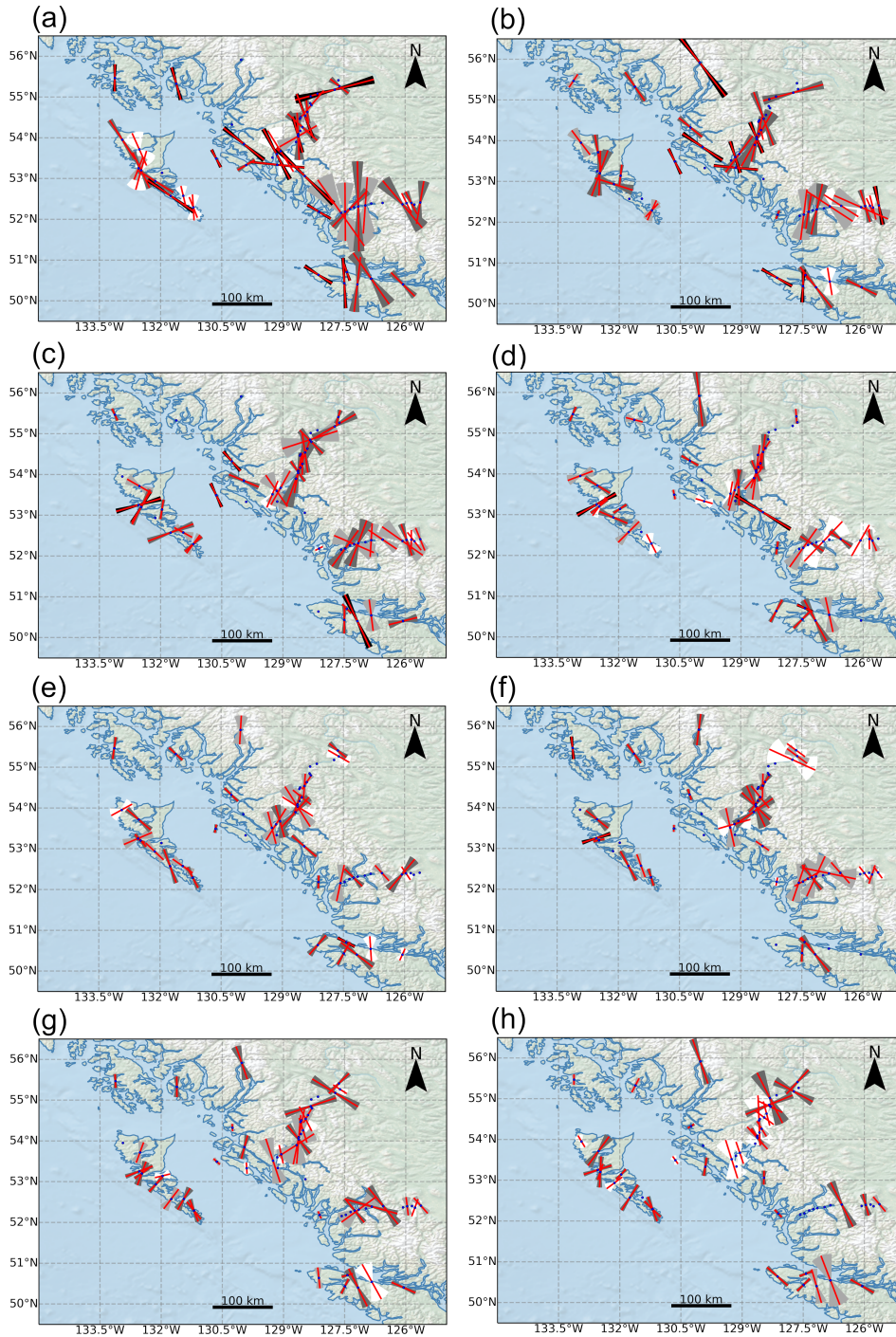


**Figure 4.** Maps of RF anisotropy for depth ranges of 5-15 km (a), 10-20 km (b), 15-25 km (c), 20-30 km (d), 25-35 km (e), 30-40 km (f), 35-45 km (g), and 40-50 km (h). The red bars show the orientation of the  $\alpha$  estimates, which represent the strike of dipping structure or the trend of a plunging axis of hexagonal anisotropy. The red bars are scaled relative to the variance of the  $B_{\perp}$  component over the corresponding depth range. The bowties show the  $1 - \sigma$  uncertainty, shaded by magnitude, darker shading indicates smaller uncertainty.

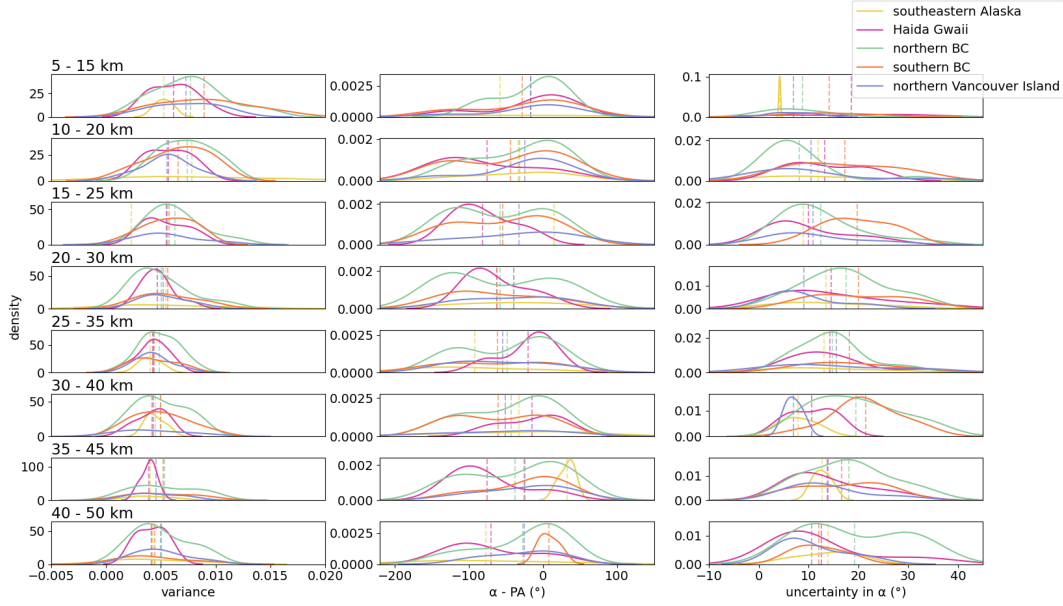


**Figure 5.** Plot showing the kernel density estimates of the  $B_{\perp}$  component variance, angular difference between PA plate motion and  $\alpha$ , and the angular uncertainty on  $\alpha$ . Plots are colored according to station sub-region, and are ordered by increasing depth. Mean values for each sub-region are plotted as vertical dashed lines.

329 At shallow depths, orientations are sub-parallel to PA plate motion, then transition to  
 330 sub-perpendicular (Fig. 5). Below 25 km,  $\alpha$  values for the northern and southern BC groups  
 331 have higher uncertainties due to a lower azimuthal coverage in the RF data at these sta-  
 332 tions compared to stations from permanent networks (Fig. 4). These regions also exhibit  
 333 a broader distribution in  $\alpha$  (Fig. 5). In general, the northern BC subset displays the most  
 334 variability in dominant RF orientations (Fig. 5). Only for the depth range of 20 - 30 km  
 335 do we see a coherent signal in this sub-region where the majority of the  $\alpha$  estimates align  
 336 approximately N-S. The overall trend in  $\alpha$  values on northern Vancouver Island do not  
 337 vary significantly across different depth ranges and show a NNW-SSE orientation (0-45  
 338 degrees clockwise from the PA plate motion).

339 In general, relative magnitudes in the measured seismic anisotropy (i.e., the vari-  
 340 ance of  $B_{\perp}$ , shown by the red bars in Figure 4 are large at all depth ranges considered,  
 341 but are greatest for the shallower depth ranges (Fig. 5). Magnitudes are the smallest on  
 342 the mainland and northern Vancouver Island for the 25 - 35 km depth range, and small-  
 343 est on Haida Gwaii for the 35 - 45 km depth range. Stations further inland tend to have

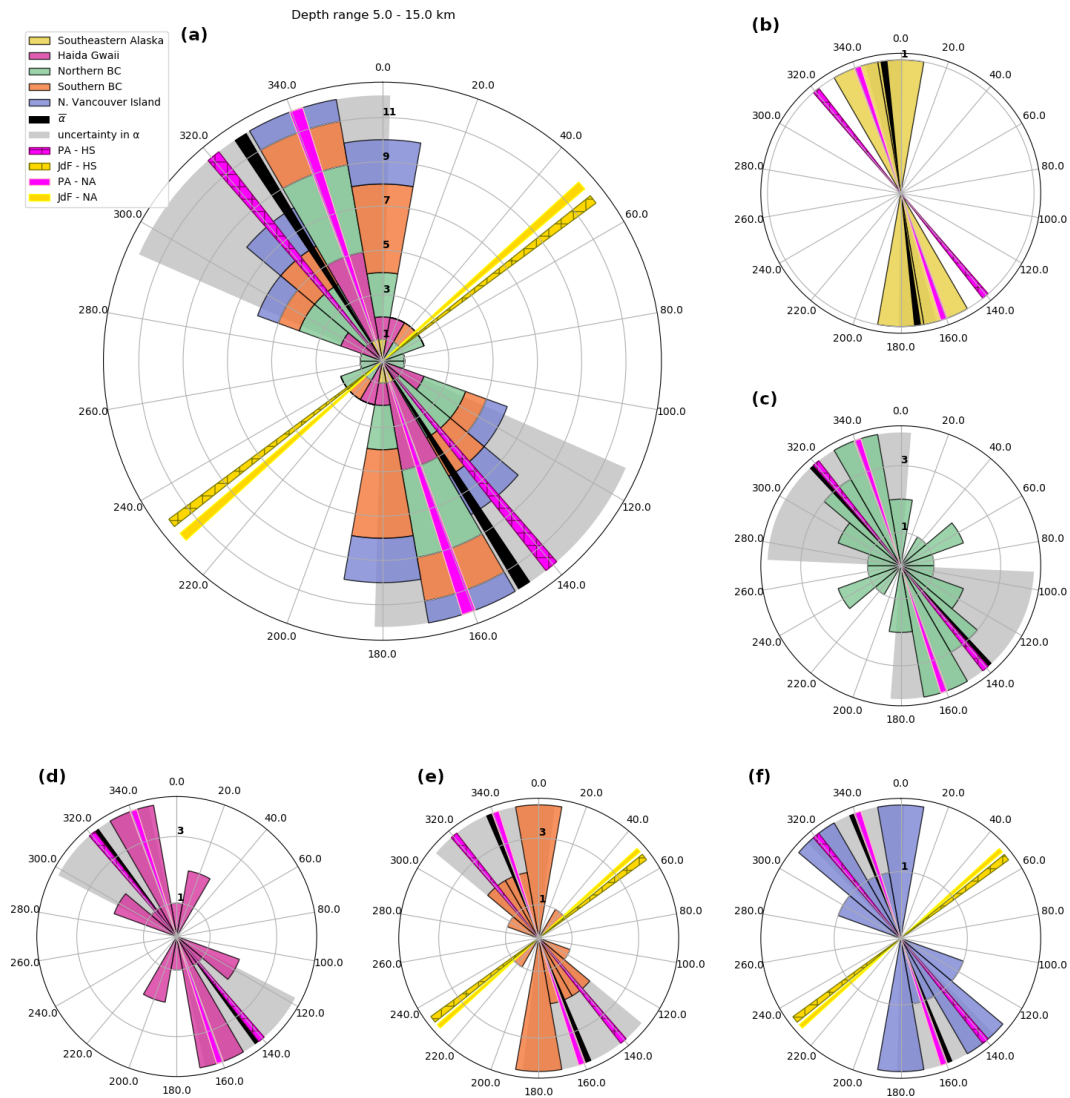


**Figure 6.** Rose diagrams showing the optimal orientations of the RFs for the 5 - 15 km depth range from Figure 4(a). Results are shown for (a) all stations, (b) southeastern Alaska, (c) Haida Gwaii, (d) northern BC, (e) southern BC, and (f) northern Vancouver Island. The circular mean angles are plotted as thick black lines with the standard deviation shown in light gray on each subplot. The directions of the PA and JdF plates relative to NA are plotted in pink and yellow respectively (Kremer et al., 2014). The directions of the PA and JdF plates relative to the global hotspot reference frame are plotted with a hatch pattern in pink and yellow respectively (Gripp & Gordon, 2002).

344 smaller magnitudes. Stations on Haida Gwaii closer to the margin have larger magni-  
345 tudes. Stations on northern Vancouver Island that lie past the approximate landward  
346 extent of the JdF slab have smaller magnitudes for most depth windows. Stations in south-  
347 eastern Alaska have largest magnitudes for the 10 - 20 km and 20 - 30 km depth ranges.

## 348 **5 Discussion**

349 Anisotropy in RFs can arise from structural heterogeneity (e.g., dipping bound-  
350 aries) and/or material anisotropy (Porter et al., 2011). These two sources of anisotropy  
351 produce similar signals in RF data and discriminating between them can prove challeng-  
352 ing (Porter et al., 2011; Schulte-Pelkum & Mahan, 2014; Audet, 2015; Tarayoun et al.,  
353 2017), especially when both are present beneath a receiver. Structural heterogeneity caused  
354 by dipping structures at the km scale are expected in a geologically complex area such  
355 as the Haida Gwaii and Cascadia margins where large dipping faults exist, but also be-  
356 neath major terrane boundaries in the form of Moho offsets or Moho dip, and as large-  
357 scale intrusions such as sill-like plutons (Rubin & Saleeby, 1992; Morozov et al., 2001;  
358 Hollister & Andronicos, 2006; Calkins et al., 2010). Material anisotropy is expected from  
359 pervasive micro-fracturing in the brittle crust due to the regional stress field (Crampin,  
360 1994; Balfour et al., 2012), or through the coherent alignment of anisotropic minerals due  
361 to past or present deformation processes. Below we compare our anisotropy estimates  
362 with previous results and with expectations for both structural heterogeneity and ma-  
363 terial anisotropy. It should be noted that our analysis focuses on RF signatures due to  
364 anisotropy with a plunging axis of symmetry and/or dipping structures. Hence, this rep-  
365 represents a possible source of discrepancy between our observations and previous studies  
366 that consider purely azimuthal anisotropy. We follow this comparison with a discussion  
367 of the implications of our observations for the structure of the crust in western Canada.

### 368 **5.1 Comparison with previous anisotropy studies**

369 RFs sample structure and anisotropy nearly vertically beneath recording stations.  
370 Other passive seismic methods that resolve crustal seismic anisotropy include shear-wave  
371 splitting from local earthquakes, and surface-wave tomography (at appropriate periods).  
372 Cao et al. (2017) estimated crustal seismic anisotropy using local shear-wave splitting  
373 estimated at five stations on Haida Gwaii. They generally found fast-axis directions sub-  
374 perpendicular to the maximum compressive stress direction, and attributed the crustal

375 anisotropy to structural fabrics arising from local geological features that have yet to be  
376 studied/identified. Interestingly, our results at the specific stations used by Cao et al.  
377 (2017) do not agree and show orientations either margin-parallel or sub-parallel to the  
378 maximum compressive stress (within the range of uncertainties) for our shallowest depth  
379 range. Such differences may arise from a number of effects, such as the averaging over  
380 a larger volume sampled by the regional S waves, the different depth sensitivity, and the  
381 small number of events considered in shear-wave splitting that resulted in only one well-  
382 constrained splitting estimate (Cao et al., 2017). This may suggest the presence of mul-  
383 tiple sources of anisotropy and/or dipping structures beneath these sites.

384 Local shear-wave splitting was performed by Balfour et al. (2012) over the south-  
385 ern half of Vancouver Island and surrounding area. The splitting analysis from the ma-  
386 jority of stations yielded a fast-axis aligned with the strike of the JdF-NA margin but  
387 results further northeast were approximately margin-perpendicular. These results were  
388 attributed to anisotropy in the upper crust caused by maximum compressive stress-aligned  
389 fluid-filled microcracks. Their results from stations along the western coast of Vancou-  
390 ver Island did not align with maximum compressive stress and instead were attributed  
391 to the long-term stress state caused by margin-parallel deformation. On the west coast  
392 of northern Vancouver Island, we find  $\alpha$  aligned margin-parallel at shallow depths. Mov-  
393 ing inland from the margin, the orientation of the fast-axis transitions to values simi-  
394 lar to the maximum compressive stress direction (Balfour et al., 2011) but then rotates  
395 back towards margin-parallel, in agreement with Balfour et al. (2012). The margin-parallel  
396 stresses  $\sim 150$  km east of the margin reflects the residual strain caused by the northward  
397 push of the rotating Oregon Block (Balfour et al., 2012).

398 Gosselin et al. (2020) mapped the fast-axis orientation of azimuthal anisotropy from  
399 Rayleigh-wave group-velocity dispersion data over western Canada and northwestern United  
400 States. Fast-axis directions were found to be margin-parallel between Vancouver Island  
401 and Haida Gwaii. From the southeast to northwest they also observed a slight rotation  
402 and change in magnitude of fast-axis orientations. These results were consistent for Rayleigh-  
403 wave group velocity periods from 15 to 50 s, which are sensitive down to  $\sim 80$  km. The  
404 estimated fast-axis directions on Haida Gwaii were perpendicular to the maximum com-  
405 pressive stress found by Ristau et al. (2007) and thus attributed to structural foliations  
406 whereas fast-axis results elsewhere in the study region were attributed to maximum com-  
407 pressive stress-aligned fluid filled cracks and/or fabrics associated with tectonic assem-

408 bly of the margin. The observed rotation in anisotropy orientations between Vancouver  
409 Island and Haida Gwaii was attributed to the transitional tectonic regime along the coast  
410 (Gosselin et al., 2020). We observe this rotation in the dominant RF orientations in the  
411 5 - 15 km and 25 - 35 km depth ranges only. Surface waves are sensitive to bulk prop-  
412 erties integrated over a wide depth range (for a given period). It is likely that our RF  
413 analysis is sensitive to discontinuous structures as well as bulk properties that are also  
414 reflected in the surface wave data. Our results within 25 - 35 km depth likely encompasses  
415 the Moho, and is likely too deep to be attributable to crustal microcracks. Additionally,  
416 the results of the surface-wave study are obtained from a tomographic inversion with lower  
417 lateral resolution than our study at distinct individual stations.

## 418 **5.2 Structural heterogeneity**

419 Faults orientations taken from the BC Geological Survey’s geology faults database  
420 (Cui, 2014) were compared to our results on a regional and local ( $< 5$  km) scale. In gen-  
421 eral,  $\alpha$  estimates do not consistently align with terrane boundaries or fault orientations  
422 (Fig. S2) at the majority of the depth ranges considered in this study. Instead, the av-  
423 erage  $\alpha$  estimates are rotated  $>25^\circ$  clockwise from the average strike of mapped faults.  
424 Therefore, we interpret that fault structures do not represent the dominant source of BAZ  
425 variations in the RF data, but are a potential a contributing factor. Regionally, we ex-  
426 pect dipping structures associated with deformation at active plate margins to dominate  
427 the RF signal, such as potential underthrusting beneath Haida Gwaii and northern Van-  
428 couver Island (Smith et al., 2003; Bustin et al., 2007; Audet et al., 2008; Gosselin et al.,  
429 2015), or across Moho depth gradients associated with the CPC (Morozov et al., 2001;  
430 Calkins et al., 2010).

431 Over Haida Gwaii, previous RF studies inferred an eastward increase in Moho depth  
432 from  $\sim 18$  km to 26 km (Smith et al., 2003; Bustin et al., 2007; Gosselin et al., 2015), in  
433 addition to a dipping interface from  $\sim 25$  km to 40 km potentially associated with PA  
434 slab underthrusting beneath the archipelago. Such dipping structures would be expected  
435 to generate RF anisotropy with  $\alpha$  sub-parallel to the margin at those depths (Porter et  
436 al., 2011). However, the spatial distribution of  $\alpha$  estimates across Haida Gwaii does not  
437 show this pattern except for the shallowest depth range, which does not encompass ei-  
438 ther of these dipping structures (Fig. 4(a), Figure 6). Based on Moho depth estimates,  
439 we should expect to see this signal between 15 km to 30 km (Figs 4(c) and (d)). Instead,

440 we see a juxtaposition of margin-parallel and margin-perpendicular  $\alpha$ . Therefore, we do  
 441 not attribute these signals in the RF data to arise from structural heterogeneity of a dip-  
 442 ping Moho. At depth ranges associated with the underthrusting PA slab (25 km to 40 km,  
 443 Figures 4(e) and (f)), we observe  $\alpha$  orientations sub-parallel to the margin for the ma-  
 444 jority of stations on Haida Gwaii. Notably, stations further west have  $\alpha$  aligned sub-perpendicular  
 445 to the margin. At depths greater than 40 km (i.e., below the Moho), all stations except  
 446 those at the very southern tip of Haida Gwaii resolve  $\alpha$  perpendicular to the margin. These  
 447 results support a layer dipping towards the northeast beginning at approximately 25 km  
 448 depth (Smith et al., 2003; Bustin et al., 2007; Gosselin et al., 2015). Because these depths  
 449 potentially encompass both the overriding plate and underthrusting material, RF sig-  
 450 natures may reflect changes in material anisotropy above and below major tectonic con-  
 451 tacts, as suggested by the observed rotations in the  $\alpha$  values with depth (Fig. 4) and the  
 452 presence of large variance in the  $B_{\parallel}$  component of Figure 3(a).

453 On northern Vancouver Island, approximately half of the stations are located north  
 454 of the terminus of the subducting JdF slab as determined by Audet et al. (2008). Due  
 455 to the low dip angle of the JdF slab,  $\alpha$  estimates are predicted to align with the slab strike  
 456 as slab depth increases from 10 to 50 km below northern Vancouver Island. Above the  
 457 JdF slab,  $\alpha$  is rotated  $\sim 0\text{--}20^\circ$  clockwise from the margin orientation and predicted slab  
 458 strike, depending on the depth range considered. This could indicate an inaccurate slab  
 459 depth model (Audet et al., 2008) and/or the contribution of material anisotropy above  
 460 and below the JdF slab. North of the projected JdF slab,  $\alpha$  estimates remain aligned  
 461 with the margin and PA plate motion. However, we note that the relative magnitude  
 462 of seismic anisotropy is lower in this region and some depth ranges display margin-normal  
 463 orientations. This result is consistent with the absence of the JdF slab (Audet et al., 2008),  
 464 and likely reflect the effects of material anisotropy in the crust.

465 In northern BC,  $V_p/V_s$  ratios measured by Calkins et al. (2010), and seismic re-  
 466 flectors identified by Morozov et al. (1998), indicate the presence of highly felsic sill-like  
 467 plutons within the CPC and a Moho offset on the western boundary. Models proposed  
 468 by Hollister and Andronicos (2006) and Morozov et al. (1998) account for this Moho off-  
 469 set with a thrust belt on the western edge of the CPC that extends to mantle depths.  
 470 Their model also includes a ductile shear zone between the CPC and Stikinia terrane that  
 471 dips east-to-northeast to a depth of  $\sim 25$  km below Stikinia and extends  $>50$  km west  
 472 of the boundary. Each of these structural heterogeneities may be reflected in our RF anal-

473 ysis. Along the eastern edge of the Alexander terrane (Fig. 1),  $\alpha$  estimates are oriented  
474 NW-SE over all crustal depths but not below the predicted Moho depth. This supports  
475 the presence of a thrust belt through the entire crust. This feature persists into south-  
476 eastern Alaska. We also note that this structure, which was suggested to have formed  
477 prior to the mid-Cretaceous translation of the terranes (Morozov et al., 1998), does not  
478 appear to be present in the YTT. At depths associated with the Moho, which dips north-  
479 east and increases west to east from  $\sim 25$  km to  $\sim 30$  km (Calkins et al., 2010), stations  
480 within the YTT and several stations in the Stikinia terrane have  $\alpha$  values oriented N-  
481 S in contrast with the orientations in western Alexander terrane. Our limited dataset  
482 within the CPC, in addition to data from stations on the eastern edge of Stikinia, show  
483 a NE-SW alignment. For the northeast dipping Moho described by Calkins et al. (2010),  
484 we expect to see a NW-SE trend in the orientation of  $\alpha$  values. However, outside of the  
485 Alexander terrane, our results display variable orientations in  $\alpha$  at Moho depths. This  
486 may reflect complex local Moho topography rather than a consistent dipping Moho across  
487 the region. Furthermore, our results for the northern BC sub-region may be the result  
488 of a complex interplay between dipping structures from the Moho and plutons, in ad-  
489 dition to seismically anisotropic materials.

490 Along the southern BC sub-region, Calkins et al. (2010) found that the Moho dips  
491 from a depth of  $\sim 27$  km in the west to  $\sim 34$  km in the east. Uncertainties in our anal-  
492 ysis at Moho depths are significant (Fig. 4(d) and (e)). Two dominant orientations are  
493 present. However, it is challenging to identify spatial trends and the lack of high qual-  
494 ity data prohibits us from further interpretation at Moho depths along the western bound-  
495 ary of the CPC. A dipping interface at  $\sim 15$  km depth between the CPC and Stikinia ter-  
496 rane was detected by Calkins et al. (2010) in southern BC, in agreement with the duc-  
497 tile shear zone in the model proposed by Hollister and Andronicos (2006). We observe  
498 the potential effects of a dipping interface in our  $\alpha$  values for the southern BC sub-region  
499 for the 10-20 and 15-25 km depth ranges (Fig. 4(b) and (c)), where stations near the east-  
500 ern edge of the CPC have  $\alpha$  values aligned WNW-ESE, in contrast to other stations in  
501 the subset. This feature is challenging to identify in the northern BC sub-region due to  
502 a lack of high-quality data. Our results, in combination with Calkins et al. (2010), sug-  
503 gest that this dipping structure persists along the entire length of the boundary between  
504 the CPC and Stikinia.

### 5.3 Material anisotropy

Variations in the RF data with respect to BAZ are likely not explained solely by the effects of structural heterogeneity. In this section, we investigate models of material anisotropy in the crust to interpret our results. Because we estimate  $\alpha$  from the degree-one harmonic term, we consider models that produce either a plunging slow-axis or plunging fast-axis of hexagonal symmetry (e.g. Porter et al., 2011). Continental seismic anisotropy typically originates from a combination of frozen (i.e., fossil) and active tectonics (Maupin & Park, 2007). Anisotropy in seismic waves can be caused by alternating layers with significant velocity contrasts (such as sediment stratigraphy); pervasive aligned cracks within an isotropic material; alignment of anisotropic minerals within a rock; or highly foliated metamorphic rocks. Here, we do not consider sediments as a significant source of anisotropy below 5 km depth. In the upper, brittle crust, azimuthal anisotropy (i.e., horizontal symmetry axis) is usually attributed to either mineral or (possibly fluid-filled) crack alignment. This is based on the closing of micro-fractures that are not aligned with the maximum principle stress axis (Crampin, 1994), which is sub-horizontal in western Canada (Ristau et al., 2007). Hexagonal anisotropy with a tilted axis in the mid- to lower-crust is believed to result from mineral alignment or foliated rocks such as mica schists (Porter et al., 2011). In the mantle, hexagonal anisotropy can arise from the coherent alignment of olivine in peridotite (fast symmetry axis) and/or serpentinite veins (slow symmetry axis) (Watanabe et al., 2007; Reynard, 2013). The source of the anisotropy in this study must be coherent at a scale resolvable by RFs (about 1-10 km).

In southern BC, along the eastern edge of the CPC, material anisotropy in the form of siliceous and foliated mylonites within the northeast dipping ductile shear zone (Jones & Nur, 1982; Heah, 1991; Andronicos et al., 2003) may also contribute to the WNW-ESE aligned  $\alpha$  values in our results for the 10-20 and 15-25 km depth ranges (Fig. 4(b) and (c)) as the slow-axis of anisotropy.

In general, our  $\alpha$  estimates for the shallowest depth range considered (5-15 km) do not align with the maximum horizontal stress directions. Therefore, we do not interpret our results to be the reflection of fluid-filled microcracks in this region. Given that  $\alpha$  generally aligns well with the approximate strike of the QCF segment near Haida Gwaii, we attribute potential material anisotropy at shallow depths to shear-induced mineral alignment caused by the transpressive motion at the plate boundary. In the case of stations

537 with high uncertainty, the anisotropy measured may be a combination of shear-induced  
538 mineral alignments and stress oriented microcracks. Haida Gwaii and northern Vancou-  
539 ver Island both lie within the Wrangellia terrane, which is dominated by mafic and ul-  
540 tramafic rocks overlain by sediments (Shellnutt et al., 2021). Material anisotropy at up-  
541 per crustal depths may also reflect pervasive fossil fabric from veining (or dykes), or shear-  
542 induced fabric acquired during margin-parallel translation of the terrane to its current  
543 location during the late Cretaceous to early Tertiary (Chardon et al., 1999; Hollister &  
544 Andronicos, 2006).

545 For many other locations throughout our study area, stress measurements are ei-  
546 ther sparse or unavailable, and we are not able to exclude stress-induced microcracks as  
547 a source of anisotropy at shallow depths. However, the stress field is expected to be rel-  
548 atively uniform throughout western Canada (Ristau et al., 2007), and this likely does  
549 not explain the observed scatter in  $\alpha$  at short spatial scales. Our results do not show clus-  
550 tering with respect to surface geology (i.e., terrane boundaries). However, the average  
551 azimuths within the terranes are oriented  $>25^\circ$  clockwise from the average strike of crustal  
552 faults (Fig. S2), which are attributed to the translation of the terranes along the mar-  
553 gin. Therefore, we propose that the observed anisotropy may be caused by shear-induced  
554 mineral alignment during terrane emplacement (Chardon et al., 1999), which has been  
555 overprinted by the active tectonics in the region such as the slab window and the (poorly  
556 constrained) transition from subduction to transform plate boundaries from south to north  
557 (Gosselin et al., 2020).

## 558 **6 Conclusions**

559 RFs are calculated for a dataset of 74 land-based broadband seismic stations dis-  
560 tributed around the Haida Gwaii margin, in order to study seismic anisotropy at crustal  
561 depths. The RF data vary with respect to BAZ, indicating the presence of seismic anisotropy  
562 or dipping structures beneath all stations considered here. These data are further pro-  
563 cessed to estimate a dominant orientation attributable to either the strike of a dipping  
564 interface or the trend of a plunging axis of material anisotropy.

565 At the shallowest depth, we observe a coherent orientation that rotates slightly along  
566 the strike of the margin from the southeast to the northwest. Beneath Haida Gwaii, our  
567 results agree with the presence of the underthrusting PA beneath NA. Beneath north-

568 ern Vancouver Island, we detect the effects of the subducting JdF slab, and are able to  
569 differentiate between stations that are above the slab and those beyond the northern ex-  
570 tent of the JdF plate. Inland, we detect the signature of a thrust belt along the eastern  
571 boundary of the Alexander terrane. In southern BC, we detect either a dipping inter-  
572 face or material anisotropy caused by deformation between the CPC and Stikinia, which  
573 likely extends along the terrane boundary. Generally, dominant RF orientations are ro-  
574 tated clockwise from the strike of terrane boundaries and fault trends, and we attribute  
575 this to be the manifestation of fossil fabrics created during the translation of terranes  
576 overprinted by the modern active tectonics along the plate margins. The local complex-  
577 ity of our results highlights the complexity of this region.

578 This study adds additional constraint on seismic anisotropy throughout this com-  
579 plex geologic area, and provides insight into the formation of western BC and the cur-  
580 rent tectonic regime.

## 581 **Acknowledgments**

582 This project is supported by the Natural Sciences and Engineering Research Council of  
583 Canada Collaborative Research and Training Experience program (iMAGE-CREATE)  
584 on Marine Geodynamics and Georesources (TTK) and Discovery grant (PA), and a Vanier  
585 Canada Graduate Scholarship (JMG). Funding contributions have also made by the Cana-  
586 dian Exploration Geophysical Society (KEGS) foundation, the Canadian Society of Ex-  
587 ploration Geophysicists (CSEG) and the Ontario Graduate Scholarship program (TTK).  
588 This work directly contributes to the objectives of the Geological Survey of Canada's Pub-  
589 lic Safety Geoscience Program, Plate Boundary Earthquakes and Active Tectonics Ac-  
590 tivity.

591 The seismic data used for RF processing in this study are available from IRIS Fed-  
592 eration of Digital Seismograph Networks (FDSN) network identifiers for networks AT  
593 via doi: 10.7914/SN/AT (NOAA National Oceanic and Atmospheric Administration (USA),  
594 1967), TA via doi: 10.7914/SN/TA (IRIS Transportable Array, 2003), and XY via doi:  
595 10.7914/SN/XY\_2005 (Dueker & Zandt, 2005) are available at [www.iris.edu/hq/](http://www.iris.edu/hq/) and from  
596 the Canadian Hazards Information Service, Earthquakes Canada Database FDSN net-  
597 work identifiers CN via doi: 10.7914/SN/CN (Natural Resources Canada (NRCAN Canada),  
598 1975) and C8 available at [www.earthquakescanada.nrcan.gc.ca](http://www.earthquakescanada.nrcan.gc.ca). A list of earthquake event  
599 metadata used in this study is available via doi: 10.5281/zenodo.6539941 (Tracey Kyrlyliuk

600 et al., 2022). v0.2.3 of StDb used for creation of station information databases licensed  
 601 under Open copyright 2019 Andrew Schaeffer & Pascal Audet is freely available at scha-  
 602 efferaj.github.io/StDb. v0.1.0 of RfPy used for RF calculation and plotting, and harmonic  
 603 decomposition and plotting, licensed under Open Copyright 2019 Pascal Audet is avail-  
 604 able at doi: 10.5281/zenodo.4302558 (Audet, 2020).

## 605 References

- 606 Andronicos, C. L., Chardon, D. H., Hollister, L. S., Gehrels, G. E., & Woodsworth,  
 607 G. J. (2003). Strain partitioning in an obliquely convergent orogen,  
 608 plutonism, and synorogenic collapse: Coast mountains batholith, british  
 609 columbia, canada. *Tectonics*, *22*(2). Retrieved from [https://agupubs](https://agupubs.onlinelibrary.wiley.com/doi/abs/10.1029/2001TC001312)  
 610 [.onlinelibrary.wiley.com/doi/abs/10.1029/2001TC001312](https://agupubs.onlinelibrary.wiley.com/doi/abs/10.1029/2001TC001312) doi:  
 611 <https://doi.org/10.1029/2001TC001312>
- 612 Audet, P. (2015). Layered crustal anisotropy around the san andreas fault near  
 613 parkfield, california. *Journal of Geophysical Research: Solid Earth*, *120*(5),  
 614 3527-3543. Retrieved from [https://agupubs.onlinelibrary.wiley](https://agupubs.onlinelibrary.wiley.com/doi/abs/10.1002/2014JB011821)  
 615 [.com/doi/abs/10.1002/2014JB011821](https://agupubs.onlinelibrary.wiley.com/doi/abs/10.1002/2014JB011821) doi: [https://doi.org/10.1002/](https://doi.org/10.1002/2014JB011821)  
 616 [2014JB011821](https://doi.org/10.1002/2014JB011821)
- 617 Audet, P. (2020). *Rfpy: Teleseismic receiver function calculation and post-*  
 618 *processing*. Zenodo. Retrieved from [https://doi.org/10.5281/zenodo](https://doi.org/10.5281/zenodo.4302558)  
 619 [.4302558](https://doi.org/10.5281/zenodo.4302558) doi: 10.5281/zenodo.4302558
- 620 Audet, P., Bostock, M. G., Mercier, J.-P., & Cassidy, J. F. (2008). Morphology  
 621 of the Explorer–Juan de Fuca slab edge in northern Cascadia: Imaging plate  
 622 capture at a ridge-trench-transform triple junction. *Geology*, *36*(11), 895–898.
- 623 Babuska, V., & Cara, M. (1991). *Seismic anisotropy in the earth* (Vol. 10). Springer  
 624 Science & Business Media.
- 625 Balfour, N. J., Cassidy, J. F., & Dosso, S. E. (2012). Crustal anisotropy in the fore-  
 626 arc of the Northern Cascadia Subduction Zone, British Columbia. *Geophysical*  
 627 *Journal International*, *188*(1), 165-176. Retrieved from [https://doi.org/10](https://doi.org/10.1111/j.1365-246X.2011.05231.x)  
 628 [.1111/j.1365-246X.2011.05231.x](https://doi.org/10.1111/j.1365-246X.2011.05231.x) doi: 10.1111/j.1365-246X.2011.05231.x
- 629 Balfour, N. J., Cassidy, J. F., Dosso, S. E., & Mazzotti, S. (2011). Mapping crustal  
 630 stress and strain in southwest British Columbia. *Journal of Geophysical Re-*  
 631 *search*, *116*, B03314. Retrieved from <https://hal.archives-ouvertes.fr/>

- 632 hal-00853734 doi: 10.1029/2010JB008003
- 633 Bianchi, I., Park, J., Piana Agostinetti, N., & Levin, V. (2010). Mapping seismic  
634 anisotropy using harmonic decomposition of receiver functions: An application  
635 to northern apennines, italy. *Journal of Geophysical Research: Solid Earth*,  
636 115(B12). Retrieved from <https://agupubs.onlinelibrary.wiley.com/doi/abs/10.1029/2009JB007061> doi: <https://doi.org/10.1029/2009JB007061>
- 637
- 638 Bird, A. L. (1999). *Earthquakes in the queen charlotte islands region, 1982-1996*  
639 (Unpublished doctoral dissertation). National Library of Canada = Biblio-  
640 theque nationale du Canada.
- 641 Bustin, A. M. M., Hyndman, R. D., Kao, H., & Cassidy, J. F. (2007). Evidence  
642 for underthrusting beneath the Queen Charlotte Margin, British Columbia,  
643 from teleseismic receiver function analysis. *Geophysical Journal Interna-*  
644 *tional*, 171(3), 1198-1211. Retrieved from [https://doi.org/10.1111/](https://doi.org/10.1111/j.1365-246X.2007.03583.x)  
645 [j.1365-246X.2007.03583.x](https://doi.org/10.1111/j.1365-246X.2007.03583.x) doi: 10.1111/j.1365-246X.2007.03583.x
- 646 Calkins, J. A., Zandt, G., Girardi, J., Dueker, K., Gehrels, G. E., & Ducea, M. N.  
647 (2010). Characterization of the crust of the coast mountains batholith, british  
648 columbia, from p to s converted seismic waves and petrologic modeling. *Earth*  
649 *and Planetary Science Letters*, 289(1), 145-155. Retrieved from [https://](https://www.sciencedirect.com/science/article/pii/S0012821X09006463)  
650 [www.sciencedirect.com/science/article/pii/S0012821X09006463](https://www.sciencedirect.com/science/article/pii/S0012821X09006463) doi:  
651 <https://doi.org/10.1016/j.epsl.2009.10.037>
- 652 Canadian Hazards Information Service. (2021). velocity model vel06 (continental  
653 haida gwaii) used for the national earthquake database.
- 654 Cao, L., Kao, H., & Wang, K. (2017). Contrasting upper-mantle shear wave  
655 anisotropy across the transpressive queen charlotte margin. *Tectono-*  
656 *physics*, 717, 311-320. Retrieved from [https://www.sciencedirect.com/](https://www.sciencedirect.com/science/article/pii/S0040195117303074)  
657 [science/article/pii/S0040195117303074](https://www.sciencedirect.com/science/article/pii/S0040195117303074) doi: [https://doi.org/10.1016/](https://doi.org/10.1016/j.tecto.2017.07.025)  
658 [j.tecto.2017.07.025](https://doi.org/10.1016/j.tecto.2017.07.025)
- 659 Cassidy, J. F. (1992). Numerical experiments in broadband receiver function analy-  
660 sis. *Bulletin of the Seismological Society of America*, 82, 1453—1474.
- 661 Cassidy, J. F., Rogers, G. C., & Hyndman, R. D. (2014). An overview of the 28 oc-  
662 tober 2012 m w 7.7 earthquake in haida gwaii, canada: a tsunamigenic thrust  
663 event along a predominantly strike-slip margin. *Pure and Applied Geophysics*,  
664 171(12), 3457–3465.

- 665 Chardon, D., Andronicos, C. L., & Hollister, L. S. (1999). Large-scale trans-  
 666 pressive shear zone patterns and displacements within magmatic arcs: The  
 667 coast plutonic complex, british columbia. *Tectonics*, *18*(2), 278–292. doi:  
 668 10.1029/1998TC900035
- 669 Cook, F., White, D., Jones, A., Eaton, D., Hall, J., & Clowes, R. (2010). How the  
 670 crust meets the mantle: Lithoprobe perspectives on the mohorovii disconti-  
 671 nuity and crust-mantle transition. *Canadian Journal of Earth Sciences*, *47*,  
 672 315-351. doi: 10.1139/E09-076
- 673 Crampin, S. (1994). The fracture criticality of crustal rocks. *Geophysical Journal In-*  
 674 *ternational*, *118*(2), 428-438. Retrieved from [https://onlinelibrary.wiley](https://onlinelibrary.wiley.com/doi/abs/10.1111/j.1365-246X.1994.tb03974.x)  
 675 [.com/doi/abs/10.1111/j.1365-246X.1994.tb03974.x](https://onlinelibrary.wiley.com/doi/abs/10.1111/j.1365-246X.1994.tb03974.x) doi: [https://doi.org/](https://doi.org/10.1111/j.1365-246X.1994.tb03974.x)  
 676 [10.1111/j.1365-246X.1994.tb03974.x](https://doi.org/10.1111/j.1365-246X.1994.tb03974.x)
- 677 Cui, Y. (2014). (2018th ed.). Retrieved from [https://catalogue.data.gov.bc.ca/](https://catalogue.data.gov.bc.ca/dataset/geology-faults)  
 678 [dataset/geology-faults](https://catalogue.data.gov.bc.ca/dataset/geology-faults)
- 679 DeMets, C., & Dixon, T. H. (1999). New kinematic models for pacific-north amer-  
 680 ica motion from 3 ma to present, i: Evidence for steady motion and biases  
 681 in the nuvel-1a model. *Geophysical Research Letters*, *26*(13), 1921-1924.  
 682 Retrieved from [https://agupubs.onlinelibrary.wiley.com/doi/abs/](https://agupubs.onlinelibrary.wiley.com/doi/abs/10.1029/1999GL900405)  
 683 [10.1029/1999GL900405](https://agupubs.onlinelibrary.wiley.com/doi/abs/10.1029/1999GL900405) doi: <https://doi.org/10.1029/1999GL900405>
- 684 DeMets, C., Gordon, R. G., & Argus, D. F. (2010). Geologically current plate  
 685 motions. *Geophysical Journal International*, *181*(1), 1-80. Retrieved  
 686 from <https://doi.org/10.1111/j.1365-246X.2009.04491.x> doi:  
 687 [10.1111/j.1365-246X.2009.04491.x](https://doi.org/10.1111/j.1365-246X.2009.04491.x)
- 688 Dueker, K., & Zandt, G. (2005). *Magma accretion and the formation of*  
 689 *batholiths*. International Federation of Digital Seismograph Networks. Re-  
 690 trieved from [https://www.fdsn.org/networks/detail/XY\\_2005/](https://www.fdsn.org/networks/detail/XY_2005/) doi:  
 691 [10.7914/SN/XY\\_2005](https://doi.org/10.7914/SN/XY_2005)
- 692 Engebretson, D. C., Cox, A., & Gordon, R. G. (1984). Relative motions be-  
 693 tween oceanic plates of the pacific basin. *Journal of Geophysical Re-*  
 694 *search: Solid Earth*, *89*(B12), 10291-10310. Retrieved from [https://](https://agupubs.onlinelibrary.wiley.com/doi/abs/10.1029/JB089iB12p10291)  
 695 [agupubs.onlinelibrary.wiley.com/doi/abs/10.1029/JB089iB12p10291](https://agupubs.onlinelibrary.wiley.com/doi/abs/10.1029/JB089iB12p10291)  
 696 doi: <https://doi.org/10.1029/JB089iB12p10291>
- 697 Gabrielse, H., Monger, J. W. H., Wheeler, J. O., & Yorath, C. J. (1991). Part a:

- 698 Morphogeological belts, tectonic assemblages and terranes [chapter 2: Tectonic  
699 framework]. In (Vol. G-2, p. 15/28). doi: <https://doi.org/10.4095/134069>
- 700 Gosselin, J. M., Audet, P., Schaeffer, A. J., Darbyshire, F. A., & Estève, C. (2020).  
701 Azimuthal anisotropy in Bayesian surface wave tomography: application to  
702 northern Cascadia and Haida Gwaii, British Columbia. *Geophysical Journal  
703 International*, *224*(3), 1724-1741. Retrieved from [https://doi.org/10.1093/  
704 gji/ggaa561](https://doi.org/10.1093/gji/ggaa561) doi: 10.1093/gji/ggaa561
- 705 Gosselin, J. M., Cassidy, J. F., & Dosso, S. E. (2015). Shear-wave velocity struc-  
706 ture in the vicinity of the 2012 mw 7.8 haida gwaii earthquake from receiver  
707 function inversion. *Bulletin of the Seismological Society of America*, *105*(2B),  
708 1106–1113. doi: 10.1785/0120140171
- 709 Gripp, A. E., & Gordon, R. G. (2002). Young tracks of hotspots and current plate  
710 velocities. *Geophysical Journal International*, *150*(2), 321-361. Retrieved from  
711 <https://doi.org/10.1046/j.1365-246X.2002.01627.x> doi: 10.1046/j.1365  
712 -246X.2002.01627.x
- 713 Hammer, P. T.-C., Clowes, R. M., & Ellis, R. M. (2000). Crustal structure  
714 of NW British Columbia and SE Alaska from seismic wide-angle stud-  
715 ies: Coast Plutonic Complex to Stikinia. *JGR*, *105*(B4), 7961-7981. doi:  
716 10.1029/1999JB900378
- 717 Heah, T. S. T. (1991). Mesozoic ductile shear and paleogene extension along the  
718 eastern margin of the central gneiss complex, coast belt, shames river area,  
719 near terrace, british columbia..
- 720 Hollister, L. S., & Andronicos, C. L. (2006). Formation of new continental crust  
721 in western british columbia during transpression and transtension. *Earth  
722 and Planetary Science Letters*, *249*(1), 29-38. Retrieved from [https://  
723 www.sciencedirect.com/science/article/pii/S0012821X06004857](https://www.sciencedirect.com/science/article/pii/S0012821X06004857) doi:  
724 <https://doi.org/10.1016/j.epsl.2006.06.042>
- 725 Hyndman, R. D. (2015). Tectonics and structure of the queen charlotte fault zone,  
726 haida gwaii, and large thrust earthquakes. *Bulletin of the Seismological Society  
727 of America*, *105*(2B), 1058–1075.
- 728 Hyndman, R. D., & Ellis, R. M. (1981). Queen charlotte fault zone: mi-  
729 croearthquakes from a temporary array of land stations and ocean bottom  
730 seismographs. *Canadian Journal of Earth Sciences*, *18*(4), 776-788. Retrieved

- 731 from <https://doi.org/10.1139/e81-071> doi: 10.1139/e81-071
- 732 IRIS Transportable Array. (2003). *Usarray transportable array*. International Fed-  
 733 eration of Digital Seismograph Networks. Retrieved from [https://www.fdsn](https://www.fdsn.org/networks/detail/TA/)  
 734 [.org/networks/detail/TA/](https://www.fdsn.org/networks/detail/TA/) doi: 10.7914/SN/TA
- 735 Jones, T., & Nur, A. (1982). Seismic velocity and anisotropy in mylonites and the  
 736 reflectivity of deep crystal fault zones. *Geology*, *10*(5), 260. doi: 10.1130/0091  
 737 -7613(1982)10<textless{}260:SVAAIM<textgreater{}2.0.CO;2
- 738 Kennett, B. L. N., & Engdahl, E. R. (1991). *iasp91 velocity model*. Retrieved from  
 739 [www.iaspei.org/projects/projects.html](http://www.iaspei.org/projects/projects.html) doi: [https://doi.org/10.17611/](https://doi.org/10.17611/DP/9991809)  
 740 [DP/9991809](https://doi.org/10.17611/DP/9991809)
- 741 Kreemer, C., Blewitt, G., & Klein, E. C. (2014). A geodetic plate motion and  
 742 global strain rate model. *Geochemistry, Geophysics, Geosystems*, *15*(10), 3849-  
 743 3889. Retrieved from [https://agupubs.onlinelibrary.wiley.com/doi/abs/](https://agupubs.onlinelibrary.wiley.com/doi/abs/10.1002/2014GC005407)  
 744 [10.1002/2014GC005407](https://agupubs.onlinelibrary.wiley.com/doi/abs/10.1002/2014GC005407) doi: <https://doi.org/10.1002/2014GC005407>
- 745 Langston, C. A. (1977). The effect of planar dipping structure on source and re-  
 746 ceiver responses for constant ray parameter. *Bulletin of the Seismological Soci-*  
 747 *ety of America*, *67*(4), 1029-1050. Retrieved from [https://doi.org/10.1785/](https://doi.org/10.1785/BSSA0670041029)  
 748 [BSSA0670041029](https://doi.org/10.1785/BSSA0670041029) doi: 10.1785/BSSA0670041029
- 749 Langston, C. A. (1979). Structure under mount rainier, washington, inferred from  
 750 teleseismic body waves. *Journal of Geophysical Research: Solid Earth*, *84*(B9),  
 751 4749-4762. Retrieved from [https://agupubs.onlinelibrary.wiley.com/](https://agupubs.onlinelibrary.wiley.com/doi/abs/10.1029/JB084iB09p04749)  
 752 [doi/abs/10.1029/JB084iB09p04749](https://agupubs.onlinelibrary.wiley.com/doi/abs/10.1029/JB084iB09p04749) doi: [https://doi.org/10.1029/](https://doi.org/10.1029/JB084iB09p04749)  
 753 [JB084iB09p04749](https://doi.org/10.1029/JB084iB09p04749)
- 754 Lay, T., Ye, L., Kanamori, H., Yamazaki, Y., Cheung, K. F., Kwong, K., & Koper,  
 755 K. D. (2013). The october 28, 2012 mw 7.8 haida gwaii underthrusting  
 756 earthquake and tsunami: Slip partitioning along the queen charlotte fault  
 757 transpressional plate boundary. *Earth and Planetary Science Letters*, *375*,  
 758 57-70. Retrieved from [https://www.sciencedirect.com/science/article/](https://www.sciencedirect.com/science/article/pii/S0012821X13002434)  
 759 [pii/S0012821X13002434](https://www.sciencedirect.com/science/article/pii/S0012821X13002434) doi: <https://doi.org/10.1016/j.epsl.2013.05.005>
- 760 Leonard, L., & Bednarski, J. (2014). Field survey following the 28 october 2012  
 761 haida gwaii tsunami. *Pure and Applied Geophysics*, *171*(12), 3467-3482.
- 762 Levin, V., & Park, J. (1997). Crustal anisotropy in the ural mountains foredeep  
 763 from teleseismic receiver functions. *Geophysical Research Letters*, *24*(11),

764 1283–1286.

765 Maupin, V., & Park, J. (2007). 1.09 - theory and observations – wave prop-  
 766 agation in anisotropic media. In G. Schubert (Ed.), *Treatise on geo-*  
 767 *physics* (p. 289-321). Amsterdam: Elsevier. Retrieved from [https://](https://www.sciencedirect.com/science/article/pii/B9780444527486000079)  
 768 [www.sciencedirect.com/science/article/pii/B9780444527486000079](https://www.sciencedirect.com/science/article/pii/B9780444527486000079)  
 769 doi: <https://doi.org/10.1016/B978-044452748-6.00007-9>

770 McCaffrey, R., Long, M. D., Goldfinger, C., Zwick, P. C., Nabelek, J. L., John-  
 771 son, C. K., & Smith, C. (2000). Rotation and plate locking at the southern  
 772 cascadia subduction zone. *Geophysical Research Letters*, *27*(19), 3117-3120.  
 773 Retrieved from [https://agupubs.onlinelibrary.wiley.com/doi/abs/](https://agupubs.onlinelibrary.wiley.com/doi/abs/10.1029/2000GL011768)  
 774 [10.1029/2000GL011768](https://doi.org/10.1029/2000GL011768) doi: <https://doi.org/10.1029/2000GL011768>

775 Monger, J. W. H. (1993). Canadian cordilleran tectonics: from geosynclines to  
 776 crustal collage. *Canadian Journal of Earth Sciences*, *30*(2), 209-231. Retrieved  
 777 from <https://doi.org/10.1139/e93-019> doi: 10.1139/e93-019

778 Morozov, I. B., Smithson, S. B., Chen, J., & Hollister, L. S. (2001). Generation  
 779 of new continental crust and terrane accretion in southeastern alaska and  
 780 western british columbia: constraints from p- and s-wave wide-angle seismic  
 781 data (accrete). *Tectonophysics*, *341*(1), 49-67. Retrieved from [https://](https://www.sciencedirect.com/science/article/pii/S0040195101001901)  
 782 [www.sciencedirect.com/science/article/pii/S0040195101001901](https://www.sciencedirect.com/science/article/pii/S0040195101001901) doi:  
 783 [https://doi.org/10.1016/S0040-1951\(01\)00190-1](https://doi.org/10.1016/S0040-1951(01)00190-1)

784 Morozov, I. B., Smithson, S. B., Hollister, L. S., & Diebold, J. B. (1998). Wide-angle  
 785 seismic imaging across accreted terranes, southeastern alaska and western  
 786 british columbia. *Tectonophysics*, *299*(4), 281-296. Retrieved from [https://](https://www.sciencedirect.com/science/article/pii/S004019519800208X)  
 787 [www.sciencedirect.com/science/article/pii/S004019519800208X](https://www.sciencedirect.com/science/article/pii/S004019519800208X) doi:  
 788 [https://doi.org/10.1016/S0040-1951\(98\)00208-X](https://doi.org/10.1016/S0040-1951(98)00208-X)

789 Natural Resources Canada (NRCAN Canada). (1975). *Canadian national seis-*  
 790 *mograph network*. International Federation of Digital Seismograph Networks.  
 791 Retrieved from <https://www.fdsn.org/networks/detail/CN/> doi: 10.7914/  
 792 SN/CN

793 Nelson, J. L., Colpron, M., & Goodfellow, W. D. (2007). Tectonics and metallogeny  
 794 of the british columbia, yukon and alaskan cordillera, 1.8 ga to the present.  
 795 *Mineral deposits of Canada: A synthesis of major deposit-types, District Metal-*  
 796 *logeny, the evolution of geological provinces, and exploration methods: Geolog-*

- 797            *ical Association of Canada, Mineral Deposits Division, Special Publication, 5,*  
798            755–791.
- 799    Nelson, J. L., Colpron, M., Israel, S., Bissig, T., Rusk, B. G., & Thompson, J. F. H.  
800            (2013).    The cordillera of british columbia, yukon, and alaska: tectonics and  
801            metallogeny.    *Tectonics, Metallogeny, and Discovery: The North American*  
802            *Cordillera and Similar Accretionary Settings: Society of Economic Geologists*  
803            *Special Publication, 17*, 53–109.
- 804    NOAA National Oceanic and Atmospheric Administration (USA). (1967). *National*  
805            *tsunami warning center alaska seismic network.*    International Federation  
806            of Digital Seismograph Networks.    Retrieved from [https://www.fdsn.org/](https://www.fdsn.org/networks/detail/AT/)  
807            [networks/detail/AT/](https://www.fdsn.org/networks/detail/AT/) doi: 10.7914/SN/AT
- 808    Park, J., & Levin, V.    (2000).    Receiver Functions from Multiple-Taper Spectral  
809            Correlation Estimates. *Bulletin of the Seismological Society of America, 90*(6),  
810            1507-1520.    Retrieved from <https://doi.org/10.1785/0119990122> doi: 10  
811            .1785/0119990122
- 812    Porter, R., Zandt, G., & McQuarrie, N.    (2011).    Pervasive lower-crustal seismic  
813            anisotropy in Southern California: Evidence for underplated schists and active  
814            tectonics.    *Lithosphere, 3*(3), 201-220.    Retrieved from [https://doi.org/](https://doi.org/10.1130/L126.1)  
815            [10.1130/L126.1](https://doi.org/10.1130/L126.1) doi: 10.1130/L126.1
- 816    Reynard, R. (2013).    Serpentine in active subduction zones. *Lithos, 178*, 171-185.  
817            Retrieved from [https://www.sciencedirect.com/science/article/pii/](https://www.sciencedirect.com/science/article/pii/S002449371200432X)  
818            [S002449371200432X](https://www.sciencedirect.com/science/article/pii/S002449371200432X)    (Serpentinities from mid-oceanic ridges to subduction)  
819            doi: <https://doi.org/10.1016/j.lithos.2012.10.012>
- 820    Ristau, J., Rogers, G. C., & Cassidy, J. F.    (2007).    Stress in western canada  
821            from regional moment tensor analysis.    *Canadian Journal of Earth Sci-*  
822            *ences, 44*(2), 127-148.    Retrieved from [https://www.scopus.com/inward/](https://www.scopus.com/inward/record.uri?eid=2-s2.0-34249696881&doi=10.1139%2fE06-057&partnerID=40&md5=5ee53cf96e158ac78fa0b51c5c6bffb8)  
823            [record.uri?eid=2-s2.0-34249696881&doi=10.1139%2fE06-057&partnerID=](https://www.scopus.com/inward/record.uri?eid=2-s2.0-34249696881&doi=10.1139%2fE06-057&partnerID=40&md5=5ee53cf96e158ac78fa0b51c5c6bffb8)  
824            [40&md5=5ee53cf96e158ac78fa0b51c5c6bffb8](https://www.scopus.com/inward/record.uri?eid=2-s2.0-34249696881&doi=10.1139%2fE06-057&partnerID=40&md5=5ee53cf96e158ac78fa0b51c5c6bffb8)    (cited By 60)    doi:  
825            10.1139/E06-057
- 826    Rohr, K. M. M., Scheidhauer, M., & Trehu, A. M.    (2000).    Transpression between  
827            two warm mafic plates: The queen charlotte fault revisited.    *Journal of Geo-*  
828            *physical Research: Solid Earth, 105*(B4), 8147-8172.    Retrieved from [https://](https://agupubs.onlinelibrary.wiley.com/doi/abs/10.1029/1999JB900403)  
829            [agupubs.onlinelibrary.wiley.com/doi/abs/10.1029/1999JB900403](https://agupubs.onlinelibrary.wiley.com/doi/abs/10.1029/1999JB900403)    doi:

- 830 <https://doi.org/10.1029/1999JB900403>
- 831 Rubin, C. M., & Saleeby, J. B. (1992). Tectonic history of the eastern edge of the  
832 Alexander Terrane, southeast Alaska. *Tectonics*, *11*(3), 586-602. doi: 10.1029/  
833 91TC02182
- 834 Savage, M. K. (1998a). Lower crustal anisotropy or dipping boundaries? effects on  
835 receiver functions and a case study in new zealand. *Journal of Geophysical Re-*  
836 *search: Solid Earth*, *103*(B7), 15069–15087.
- 837 Savage, M. K. (1998b). Lower crustal anisotropy or dipping boundaries? effects on  
838 receiver functions and a case study in new zealand. *Journal of Geophysical Re-*  
839 *search: Solid Earth*, *103*(B7), 15069-15087. Retrieved from [https://agupubs](https://agupubs.onlinelibrary.wiley.com/doi/abs/10.1029/98JB00795)  
840 [.onlinelibrary.wiley.com/doi/abs/10.1029/98JB00795](https://agupubs.onlinelibrary.wiley.com/doi/abs/10.1029/98JB00795) doi: [https://doi](https://doi.org/10.1029/98JB00795)  
841 [.org/10.1029/98JB00795](https://doi.org/10.1029/98JB00795)
- 842 Savard, G., Bostock, M. G., Hutchinson, J., Kao, H., Christensen, N. I., & Pea-  
843 cock, S. M. (2020). The northern terminus of cascadia subduction. *Jour-*  
844 *nal of Geophysical Research: Solid Earth*, *125*(6), e2019JB018453. Re-  
845 trieved from [https://agupubs.onlinelibrary.wiley.com/doi/abs/](https://agupubs.onlinelibrary.wiley.com/doi/abs/10.1029/2019JB018453)  
846 [10.1029/2019JB018453](https://agupubs.onlinelibrary.wiley.com/doi/abs/10.1029/2019JB018453) (e2019JB018453 10.1029/2019JB018453) doi:  
847 <https://doi.org/10.1029/2019JB018453>
- 848 Schoettle-Greene, P., Duvall, A. R., Blythe, A., Morley, E., Matthews, W., &  
849 LaHusen, S. R. (2020). Uplift and exhumation in Haida Gwaii driven by  
850 terrane translation and transpression along the southern Queen Charlotte  
851 fault, Canada. *Geology*, *48*(9), 908-912. Retrieved from [https://doi.org/](https://doi.org/10.1130/G47364.1)  
852 [10.1130/G47364.1](https://doi.org/10.1130/G47364.1) doi: 10.1130/G47364.1
- 853 Schulte-Pelkum, V., & Mahan, K. H. (2014). A method for mapping crustal defor-  
854 mation and anisotropy with receiver functions and first results from usarray.  
855 *Earth and Planetary Science Letters*, *402*, 221-233. Retrieved from [https://](https://www.sciencedirect.com/science/article/pii/S0012821X14000661)  
856 [www.sciencedirect.com/science/article/pii/S0012821X14000661](https://www.sciencedirect.com/science/article/pii/S0012821X14000661) (Spe-  
857 cial issue on USArray science) doi: <https://doi.org/10.1016/j.epsl.2014.01.050>
- 858 Shellnutt, J. G., Dostal, J., & Lee, T. Y. (2021). Linking the wrangellia flood  
859 basalts to the galápagos hotspot. *Scientific Reports*, *11*(8579). Re-  
860 trieved from <https://doi.org/10.1038/s41598-021-88098-7> doi:  
861 [10.1038/s41598-021-88098-7](https://doi.org/10.1038/s41598-021-88098-7)
- 862 Smith, A. J., Hyndman, R. D., Cassidy, J. F., & Wang, K. (2003). Structure, seis-

- 863 micity, and thermal regime of the queen charlotte transform margin. *Journal*  
 864 *of Geophysical Research: Solid Earth*, 108(B11). Retrieved from [https://](https://agupubs.onlinelibrary.wiley.com/doi/abs/10.1029/2002JB002247)  
 865 [agupubs.onlinelibrary.wiley.com/doi/abs/10.1029/2002JB002247](https://agupubs.onlinelibrary.wiley.com/doi/abs/10.1029/2002JB002247) doi:  
 866 <https://doi.org/10.1029/2002JB002247>
- 867 Tarayoun, A., Audet, P., Mazzotti, S., & Ashoori, A. (2017). Architecture of the  
 868 crust and uppermost mantle in the northern Canadian Cordillera from receiver  
 869 functions. *Journal of Geophysical Research : Solid Earth*, 122(7), 5268-5287.  
 870 Retrieved from <https://hal.archives-ouvertes.fr/hal-01685550> doi:  
 871 10.1002/2017JB014284
- 872 ten Brink, U. S., Miller, N. C., Andrews, B. D., Brothers, D. S., & Haeussler,  
 873 P. J. (2018). Deformation of the pacific/north america plate boundary at  
 874 queen charlotte fault: The possible role of rheology. *Journal of Geophys-*  
 875 *ical Research: Solid Earth*, 123(5), 4223-4242. Retrieved from [https://](https://agupubs.onlinelibrary.wiley.com/doi/abs/10.1002/2017JB014770)  
 876 [agupubs.onlinelibrary.wiley.com/doi/abs/10.1002/2017JB014770](https://agupubs.onlinelibrary.wiley.com/doi/abs/10.1002/2017JB014770) doi:  
 877 <https://doi.org/10.1002/2017JB014770>
- 878 Thorkelson, D. J., Madsen, J. K., & Sluggett, C. L. (2011). Mantle flow through the  
 879 Northern Cordilleran slab window revealed by volcanic geochemistry. *Geology*,  
 880 39(3), 267-270. Retrieved from <https://doi.org/10.1130/G31522.1> doi: 10  
 881 .1130/G31522.1
- 882 Thorkelson, D. J., & Taylor, R. P. (1989). Cordilleran slab windows. *Ge-*  
 883 *ology*, 17(9), 833-836. Retrieved from [https://doi.org/10.1130/0091-](https://doi.org/10.1130/0091-7613(1989)017<0833:CSW>2.3.CO;2)  
 884 [7613\(1989\)017<0833:CSW>2.3.CO;2](https://doi.org/10.1130/0091-7613(1989)017<0833:CSW>2.3.CO;2) doi: 10.1130/0091-7613(1989)017<0833:  
 885 CSW>2.3.CO;2
- 886 Tracey Kyryliuk, T., Audet, P., Gosselin, J. M., & Schaeffer, A. J. (2022). *Event*  
 887 *Data used in Seismic anisotropy along the Haida Gwaii margin from receiver*  
 888 *function analysis*. Zenodo. Retrieved from [https://doi.org/10.5281/](https://doi.org/10.5281/zenodo.6539941)  
 889 [zenodo.6539941](https://doi.org/10.5281/zenodo.6539941) doi: 10.5281/zenodo.6539941
- 890 Watanabe, T., Kasami, H., & Ohshima, S. (2007, 04). Compressional and shear  
 891 wave velocities of serpentinitized peridotites up to 200 mpa. *Earth Planets*  
 892 *Space*, 59, 233-244. doi: 10.1186/BF03353100